

Effects of Wavefunction Penetration into the Gate Oxide on Self-Consistent Modeling of Deep Submicron MOSFETs.



A thesis submitted to the Department of Electrical and Electronic Engineering
of
Bangladesh University of Engineering and Technology
in partial fulfillment of the requirements for the degree of
MASTER OF SCIENCE IN ELECTRICAL AND ELECTRONIC ENGINEERING

by
Mohammad Zahed Kauser

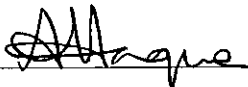
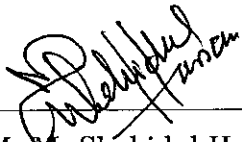

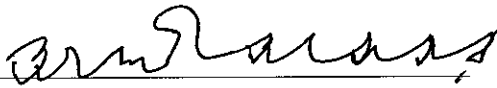


DEPARTMENT OF ELECTRICAL AND ELECTRONIC ENGINEERING
BANGLADESH UNIVERSITY OF ENGINEERING AND TECHNOLOGY

November 2001

The thesis entitled "Effects of Wavefunction Penetration into the Gate Oxide on Self-Consistent Modeling of Deep Submicron MOSFETs" submitted by Mohamad Zahed Kauser, Roll No.: 040006223P, Session: April 2000 has been accepted as satisfactory in partial fulfillment of the requirements for the degree of MASTER OF SCIENCE IN ELECTRICAL AND ELECTRONIC ENGINEERING.

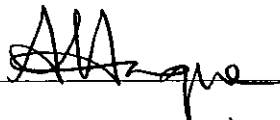
BOARD OF EXAMINERS

1.  14/11/2001 **Chairman**
(Dr. Anisul Haque)
Associate Professor
Department of Electrical and
Electronic Engineering, BUET
Dhaka-1000, Bangladesh
2. 
(Dr. M. M. Shahidul Hassan) **Member**
(Ex-officio)
Professor and Head
Department of Electrical and
Electronic Engineering, BUET
Dhaka-1000, Bangladesh
3. 
(Dr. M. Rezwan Khan) **Member**
Professor
Department of Electrical and
Electronic Engineering, BUET
Dhaka-1000, Bangladesh
4. 
(Dr. M. Ali Asgar) **Member**
(External)
Professor
Department of Physics, BUET
Dhaka-1000, Bangladesh

Declaration

I hereby declare that this thesis has been done by me and it or any part of it has not been submitted elsewhere for the award of any degree or diploma.

Signature of the supervisor



(Dr. Anisul Haque)

Associate Professor

Department of Electrical and
Electronic Engineering, BUET
Dhaka-1000, Bangladesh

Signature of the candidate



(Mohammad Zahed Kauser)

Acknowledgements

I am deeply grateful to my supervisor Dr. Anisul Haque, Associate Professor, Dept. of Electrical and Electronic Engineering, Bangladesh University of Engineering and Technology, Bangladesh, for his friendly supervision, constructive suggestions and constant support during this research, without which this work never be materialized. His guidance and continuous encouragement in every aspect of this work and my life is deeply appreciated. I am in debt with him for helping me with the facility of the solid state and simulation lab and for acquainting me with the world of advanced research.

I am grateful to Dr. M. M. Shahidul Hasan, Head of the Department of Electrical and Electronic Engineering, Bangladesh University of Engineering and Technology (BUET), Bangladesh, for his encouragement, advocacy and support by providing the microcomputer lab facilities whose outcome is the successful completion of this research. Thanks to Dr. Mohammad Ali Choudhury, Dr. M. Rezwon Khan and Dr. Kazi Mujibur Rahman for their continuous encouragement and providing me their helping hand whenever required.

Of course, I am indebted to my mother, my sisters and my wife for their encouragement, patience and love.

Dedication

To My Mother.

Contents

Acknowledgement	iii
Dedication	iv
List of Tables	vii
List of Figures	viii
Abstract	xii
1 Introduction	1
1.1 Literature Review	3
1.2 Objective of the Work	9
1.3 Organization of the Thesis	11
2 Theory	13
2.1 Existing Self-Consistent Analysis	13
2.1.1 Model	13
2.1.2 Calculation	16
2.2 Green's Function Formalism	17
2.3 Modification of Self-Consistent Analysis in the Presence of Wave Function Penetration	19
3 Results and Discussions	22
3.1 Effective mass approximation	22
3.2 n-MOS Devices on (111) silicon	24
3.3 n-MOS and p-MOS Devices for (100) silicon	33
4 Conclusion	54
4.1 Summary	54

4.2 Suggestions for Future Work	56
Bibliography	58
Appendix A	62
A.1 Brief Description of Calculation	62
A.2 Flowcharts	64

List of Tables

3.1	Effective masses of electrons in different valleys.	23
3.2	Effective masses for different types of holes.	24
3.3	Sample calculation of Δz_{avg} for electrons.	38

List of Figures

1.1	A typical conduction band profile for an n-MOSFET.	2
1.2	Electron distributions in the inversion layer of an n-MOSFET shown in Fig. 1.1.	3
3.1	Local inversion charge density, ρ_{inv} , as a function of position into silicon, z , calculated with and without considering wave function penetration. Doping density $N_A = 5 \times 10^{17} \text{ cm}^{-3}$ and oxide thick- ness $T_{ox} = 1.5 \text{ nm}$. Calculations are performed for an inversion sheet density $N_{inv} = 10^{13} \text{ cm}^{-2}$	25
3.2	Average distance of the inversion carriers from the interface, z_{avg} vs N_{inv} . $N_A = 5 \times 10^{17} \text{ cm}^{-3}$ and $T_{ox} = 1.5 \text{ nm}$	26
3.3	Relative error in z_{avg} , Δz_{avg} , as a function of N_{inv} . Calculations are for three oxide widths, $T_{ox} = 1.0 \text{ nm}$, 1.5 nm , 2.0 nm , and two doping densities, $N_A = 5 \times 10^{17} \text{ cm}^{-3}$ and 10^{18} cm^{-3}	27
3.4	Band bending ϕ_I due to inversion charge as a function of N_{inv} . $N_A = 5 \times 10^{17} \text{ cm}^{-3}$ and $T_{ox} = 1.5 \text{ nm}$	28
3.5	Relative error in ϕ_I , $\Delta\phi_I$ vs N_{inv} for $T_{ox} = 1.0 \text{ nm}$, 1.5 nm , 2.0 nm and $N_A = 5 \times 10^{17} \text{ cm}^{-3}$ and 10^{18} cm^{-3}	29
3.6	Inversion capacitance C_{inv} vs N_{inv} for $N_A = 5 \times 10^{17} \text{ cm}^{-3}$ and $T_{ox} = 1.5 \text{ nm}$	30
3.7	Relative error in C_{inv} , ΔC_{inv} , as a function of N_{inv} for $T_{ox} = 1.0$ nm , 1.5 nm , 2.0 nm and $N_A = 5 \times 10^{17} \text{ cm}^{-3}$ and 10^{18} cm^{-3}	31
3.8	Gate capacitance C_g vs V_g for (111) n-MOS. Calculations are for $N_A = 5 \times 10^{17} \text{ cm}^{-3}$ and $T_{ox} = 1 \text{ nm}$	32
3.9	Relative error in C_g , ΔC_g in (%), as a function of V_g for the device studied in Fig. 3.8.	33

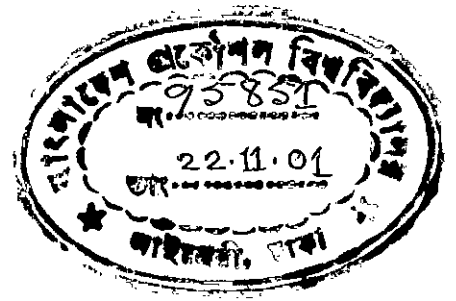
3.10	Relative errors in threshold voltage, ΔV_{TH} , and in supply voltage ΔV_{DD} , as functions of doping density N_A . Calculations are for three oxide widths $T_{ox} = 1.0$ nm, 1.5 nm, 2.0 nm.	34
3.11	Average distance of the inversion carriers from the interface, z_{avg} vs N_{inv} , for n-MOS and p-MOS, respectively. Solid lines indicate quantities with penetration and dashed lines indicate quantities without penetration. (a) for n-MOS, lines without any symbol indicate z_{avg} , lines with circle indicate z_{avgL} and lines with up-triangle indicate z_{avgT} . (b) for p-MOS, lines without any symbol indicate z_{avg} , lines with circle indicate z_{avgL} and lines with up-triangle indicate z_{avgH}	41
3.12	Relative error in z_{avg} , Δz_{avg} in nm, as a function of N_{inv} for both (a) n-MOS and (b) p-MOS, respectively. Calculations are for oxide width, $T_{ox} = 1.5$ nm and doping density, $N_A = 5 \times 10^{17}$ cm ⁻³	42
3.13	Relative error in z_{avg} , Δz_{avg} in (%), as a function of N_{inv} for both (a) n-MOS and (b) p-MOS devices, respectively. Calculations are for oxide width, $T_{ox} = 1.5$ nm and doping density, $N_A = 5 \times 10^{17}$ cm ⁻³	43
3.14	Relative concentrations of the inversion carriers in different valleys as a function of N_{inv} . Calculations are for oxide width, $T_{ox} = 1.5$ nm and doping density, $N_A = 10^{17}$ cm ⁻³ . Solid lines indicate quantities with penetration and dashed lines indicate quantities without penetration. (a) For n-MOS, lines without any symbol indicate relative concentration of longitudinal valley and lines with circle indicate relative concentration of transverse valley. (b) For p-MOS, lines without any symbol indicate relative concentration of light holes, lines with circle indicate relative concentration of heavy holes and lines with up-triangle indicate relative concentration of split-off holes.	44

3.15	Relative concentrations of the inversion carriers in different valleys as a function of N_{inv} . Calculations are for oxide width, $T_{ox}= 1.5$ nm and doping density, $N_A = 5 \times 10^{17} \text{ cm}^{-3}$. Solid lines indicate quantities with penetration and dashed lines indicate quantities without penetration. (a) For n-MOS, lines without any symbol indicate relative concentration of longitudinal valley and lines with circle indicate relative concentration of transverse valley. (b) For p-MOS, lines without any symbol indicate relative concentration of light holes, lines with circle indicate relative concentration of heavy holes and lines with up-triangle indicate relative concentration of split-off holes.	45
3.16	Relative concentrations of the inversion carriers in different valleys as a function of N_{inv} . Calculations are for oxide width, $T_{ox}= 1.5$ nm and doping density, $N_A = 10^{18} \text{ cm}^{-3}$. Solid lines indicate quantities with penetration and dashed lines indicate quantities without penetration. (a) For n-MOS, lines without any symbol indicate relative concentration of longitudinal valley and lines with circle indicate relative concentration of transverse valley. (b) For p-MOS, lines without any symbol indicate relative concentration of light holes, lines with circle indicate relative concentration of heavy holes and lines with up-triangle indicate relative concentration of split-off holes.	46
3.17	Different eigenenergies measured from Fermi energy as a function of N_{inv} . Calculations are for oxide width, $T_{ox}= 1.5$ nm and doping density, $N_A = 5 \times 10^{18} \text{ cm}^{-3}$. Solid lines indicate quantities with penetration and dashed lines indicate quantities without penetration. (a) For n-MOS and (b) For p-MOS.	47
3.18	Different eigenenergies measured from Fermi energy as a function of doping density, for (a) n-MOS and (b) p-MOS devices, respectively. Calculations are for oxide width, $T_{ox}= 1.5$ nm and inversion carrier density, $N_{inv} = 10^{12} \text{ cm}^{-2}$. Solid lines indicate quantities with penetration and dashed lines indicate quantities without penetration.	48

3.19	Inversion capacitance C_{inv} vs N_{inv} for (a) n-MOS and (b) p-MOS devices, respectively. Calculations are for, $N_A = 5 \times 10^{17} \text{ cm}^{-3}$ and $T_{ox} = 1.5 \text{ nm}$	49
3.20	Relative error in C_{inv} , ΔC_{inv} , as a function of N_{inv} for (a) n-MOS and (b) p-MOS devices, respectively. Calculations are for $T_{ox} = 1.5 \text{ nm}$ and $N_A = 10^{17} \text{ cm}^{-3}$, $5 \times 10^{17} \text{ cm}^{-3}$ and 10^{18} cm^{-3}	50
3.21	Gate capacitance C_g vs V_g for (a) n-MOS and (b) p-MOS devices, respectively. Calculation are for, $N_A = 10^{18} \text{ cm}^{-3}$ and $T_{ox} = 1 \text{ nm}$	51
3.22	Relative error in C_g , ΔC_g in (%), as a function of V_g for (a) n-MOS and (b) p-MOS respectively. Calculations are for $T_{ox} = 1 \text{ nm}$ and $N_A = 10^{17} \text{ cm}^{-3}$, $5 \times 10^{17} \text{ cm}^{-3}$ and 10^{18} cm^{-3}	52
3.23	Relative error in C_g , ΔC_g in (%), as a function of V_g for (a) n-MOS and (b) p-MOS respectively. Calculation are for $T_{ox} = 1 \text{ nm}$, 1.5 nm , 2 nm , and $N_A = 5 \times 10^{17} \text{ cm}^{-3}$	53
A.1	Flowchart.	64
A.2	Flowchart (continued).	65
A.3	Flowchart (continued).	66

Abstract

Effects of wave function penetration into gate oxide on properties of n-MOS and p-MOS devices in deep submicron regime are studied. Self-consistent modeling of MOS inversion layers is performed, taking into account the effects of wave function penetration on the solutions of both Schrödinger's and Poisson's equations. A new technique, based on Green's function formalism, has been used for the solution of Schrödinger's equation that does not require any matrix manipulation and is numerically efficient. Numerical results for n-MOS devices on (111) silicon show that the effects of wave function penetration on solution of Poisson's equation are non-trivial. Penetration effects on properties of inversion layers become more important with scaling down of device dimensions. These effects are more pronounced at strong inversion. Penetration effects on threshold voltage are found to be insignificant. However, the effects of wave function penetration on supply voltage can be as high as a few percents and these effects are weakly dependent on device scaling. Numerical results for n-MOS and p-MOS devices on (100) silicon show that the effects of wave function penetration on p-MOS devices are more severe. This is found to be due to lower effective mass of heavy holes compared to that for electrons in the longitudinal valley. Variation of doping density has opposite effects on the relative error in inversion capacitance for n-MOS and p-MOS devices. Error in gate capacitance is insignificant in the sub-threshold region and increases sharply around threshold. For n-MOS devices in strong inversion, relative error in gate capacitance decreases with increasing doping density, while that for a p-MOSFET is insensitive to doping density. Large difference in effective masses of electrons in longitudinal valley and in transverse valley compared to that of heavy and light holes are found to be responsible for this effect. Although the error in gate capacitance is only a few percent, this error will have non-trivial effects on MOSFET parameter extraction from C-V measurements. Comparison of numerical results for n-MOS structures on (111) and (100) silicon shows that penetration effects are more pronounced in n-MOSFETs on (111) silicon. This is found to be due to the lower effective mass of electron in (111) silicon.



Chapter 1

Introduction

Throughout the history of integrated circuit design, a general scaling methodology for MOSFET devices has been applied [1]. This scaling methodology relies heavily on the use of successively thinner gate dielectric and higher level of channel doping in order to simultaneously achieve the desired device turn-off and drive current capabilities as feature sizes decrease. According to the 1997 National Technology Road Map for Semiconductors (NTRS), the performance limit of a device will correspond to a channel length, $L = 100$ nm with oxide thickness of 1.5 nm and a substrate doping of $N_A = 2 \times 10^{18} \text{ cm}^{-3}$ [1]. But recently Assad *et.al.* have reported a theoretical study in which they have examined device on-current, transconductance and source to drain resistance for the ballistic limit (channel length approaching zero or the mean free path approaching infinity) and the zero oxide thickness limit [2]. They have concluded that the ultimate MOSFET limit are considerably higher than previously estimated and well above those currently achieved. Devices will have to operate significantly closer to the ballistic limit if the NTRS targets are to be met. As gate length goes below deep submicron dimensions ($\leq 0.25 \mu\text{m}$), the device design, as guided by scaling rules, can result in very large normal electric fields at the Si/SiO_2 interface, even near the threshold of inversion. This leads to a significant bending of the energy band at the Si/SiO_2 interface. It has been long known that with sufficient band bending, the potential well can become sufficiently narrow to quantize the motion of inversion layer carriers in the direction perpendicular to the interface [3]. This gives rise to a splitting of the energy levels into subbands (2-dimensional density-of-states), such that the lowest of the allowed energy levels for electrons in the well does not coincide with the bottom of the conduction band. Due to quantization,

the electron density does not reach it's maximum at the oxide-semiconductor interface as in the semi-classical model [4, 5], but instead at some distance inside the semiconductor. Fig. 1.1 shows a typical conduction profile for an n-MOSFET device and Fig. 1.2 shows the electron density in silicon near Si/SiO_2 interface as obtained from semi-classical and quantum mechanical (QM) calculations.

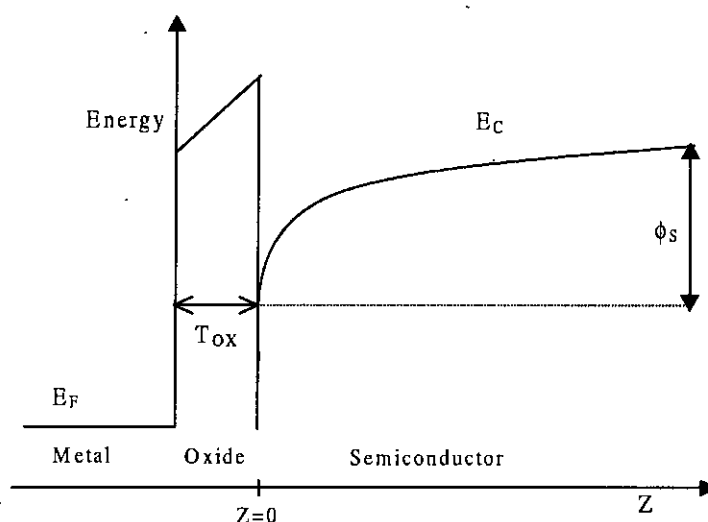


Fig. 1.1: A typical conduction band profile for an n-MOSFET.

Due to this extension of the electron density inside semiconductor, (i) the electric potential value at the interface is greater and (ii) the capacitance and the transconductance are reduced from those predicted by the semi-classical model. At room temperature in deep submicron devices, the QM effects manifest themselves through such measurable device parameters as the inversion layer charge density, threshold voltage and the oxide thickness extracted from capacitance vs. voltage (C-V) or tunneling current measurement.

Thus, it is important that the above mentioned inversion layer QM effects are accounted for in deep submicron device models. The use of the traditional or semi-classical models [4, 5] in device analysis and design, in which these effects are neglected, is inadequate at deep submicron dimensions and will lead to erroneous and misleading prediction of device structure and electrical behaviour,

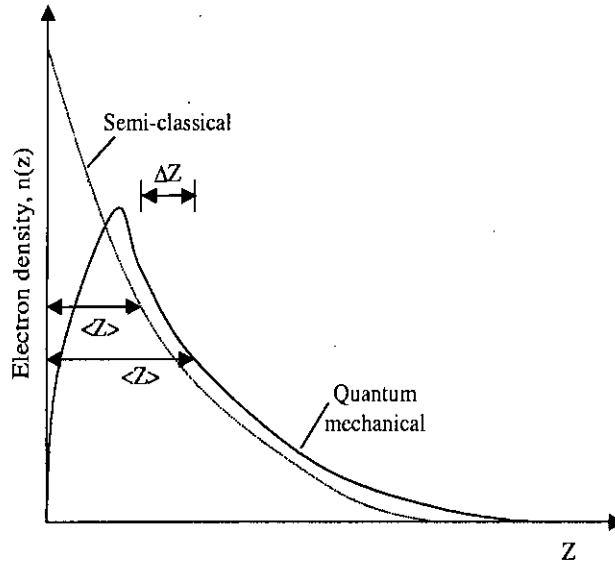


Fig. 1.2: Electron distributions in the inversion layer of an n-MOSFET shown in Fig. 1.1.

such as the physical oxide thickness, threshold voltage, drive current, gate capacitance, on-state series resistance and polysilicon workfunction. For this reason, the two-dimensional nature of electrons in inversion layers is studied in detail by considering quantization of carrier energies.

1.1 Literature Review

QM effects in MOS inversion layers arise when high surface electric field makes the quantum well for inversion carriers very steep and narrow, such that the electron energies are quantized in the direction normal to the interface. A significant amount of work has been conducted to understand and model the QM effects in MOS devices. In this section, a partial review of these works is presented.

Stern first reported the detail formulation of self-consistent modeling for n-type silicon inversion layer [3], where he solved coupled Schrödinger's and Poisson's equation iteratively. In that calculation, the author made several approximations, *e.g.*, effective mass approximation instead of periodic lattice potential, the wavefunction vanishing at the Si/SiO_2 interface and the potential well being

triangular. For a triangular potential well, the solution of Schrödinger's equation is the Airy function which he used in his self-consistent formulation. In that work, he presented numerical results for different surface orientations, bulk carrier concentrations, temperature and inversion layer carrier concentrations to understand the importance of QM effects on inversion layer parameters such as the average penetration of inversion layer charge density from the surface, z_{avg} and distribution of carriers among the subbands.

A triangular potential well is not consistent with a high density of inversion carriers. Later, Moglestue overcame many of the shortcomings of Stern's formulation and determined the wave functions self-consistently from Schrödinger's and Poisson's equations for populated subbands, using the Fermi-Dirac statistics [6]. He calculated different results for both electrons and holes for the $\langle 100 \rangle$ silicon at the interface. He compared the self-consistently obtained results with those obtained with the triangular potential well approximation. It was shown that for weak inversion, the self-consistent results do not deviate significantly from those obtained assuming triangular potential well, but for strong inversion, the carriers tend to move closer to the oxide. Thus he showed that the Airy function solution becomes inadequate and a self-consistent solution is required in strong inversion for the analysis of small transistor in VLSI applications. He also calculated gate capacitance and found that the self-consistently calculated values agree with the experimental data.

In their pioneering work, Dort *et. al.* proposed a simple model for explaining measurements in the high doping level regime where the conventional model fails to reproduce the experimental results [7]. The model proposed by them uses the same drift-diffusion approximation used by the semi-classical model [4, 5], however some advanced physics is built in the simulators. This model modifies the intrinsic carrier concentration for the silicon band gap inversion conditions. They showed that their model agreed with the results given by self-consistent calculation.

It is known that self-consistent solution of coupled Schrödinger's and Pois-

son's equations are numerically intensive and time consuming. Hareland *et. al.* proposed a new computationally efficient model for predicting QM effects on the inversion layer charge density and charge distribution [8]. Their model utilizes analytical descriptions for the first three subbands of a 2-D density-of-states in a quantized electron inversion layer. This model, along with the one proposed by Dort *et. al.* [7], has been implemented in a device simulator software named PISCES. They have shown that the inversion layer charge distribution and sub-band energies predicted by the three-subband model agree very well with the results obtained by self-consistent calculations.

Paasch *et. al.* studied the effects of influence of inversion channel quantization on surface potential [9]. They showed that the semi-classical description gives erroneous results while calculating the surface potential or the total band bending. They have shown that the error introduced in the calculation of surface potential is up to some tenth of a volt with decreasing oxide width and increasing gate voltage.

An important parameter for the MOS devices is the gate capacitance. Accurate determination of the capacitance-voltage (C-V) characteristics is essential for a MOS device as the transconductance is dependent on the gate capacitance [5]. Moreover, a correct simulation of C-V curves is very important for MOS system parameter extraction [10]. Main MOS parameters which can be obtained from C-V measurement are oxide thickness, substrate and poly-Si doping etc. If an accurate model is developed, then a good agreement between measured C-V curve and simulated C-V curve confirms the correct estimation of the parameters.

Another important parameter for submicron MOSFETs is the inversion layer capacitance, C_{inv} . Takagi *et. al.* experimentally and theoretically studied C_{inv} with emphasis on the surface carrier concentration, N_s [11]. They found that at lower N_s , C_{inv} is determined by the finite density-of-states, while, at higher N_s , C_{inv} is determined by the finite inversion-layer thickness. They have shown that C_{inv} is dependent on surface orientation in higher N_s compared to lower N_s which strengthens the above claim. They have also shown that the self-consistently cal-

culated C_{inv} accurately represents the experimental C_{inv} . It is found that an increase in substrate impurity concentration leads to an increase in C_{inv} . Finally results showed that the reduction of gate capacitance due to C_{inv} becomes more severe with decrease in the oxide thickness and this reduction is more severe in low N_s . Takagi *et. al.* also experimentally and theoretically studied C_{inv} in p-channel silicon MOSEFT's with emphasis on the surface carrier concentration, N_s [12]. They have found that the electrical gate oxide thickness is larger for inversion-layer holes than for inversion-layer electrons, because of the smaller values of C_{inv} for inversion-layer holes. An important finding of their work is that the calculation using the effective mass at the valance band edge can accurately represent the experimental results for p-MOSFETs over a whole range of N_s .

Another important quantity which is affected by the QM effects is the supply voltage. The influence of inversion-layer capacitance, C_{inv} on supply voltage, V_{dd} of n- and p-MOSEFT's is quantitatively examined by Takagi *et. al.* [13]. They have shown that the band bending of a silicon substrate in the inversion condition due to C_{inv} remain unaffected with reduction of gate oxide thickness. To accurately evaluate the band bending, they used the one-dimensional (1-D) self-consistent calculation including 2-D subband structure of inversion layer electrons and holes. As V_{dd} is defined as gate voltage to induce sufficient carriers to keep the current drive, they have found that the influence of band bending due to C_{inv} makes the operation with less than a certain value of supply voltage quite difficult, even for extremely thin gate oxide thickness.

Fiegna *et. al.* have analyzed the effects on gate capacitance, threshold voltages, effective mobility of electrons of nonuniformly doped MOS structures [14]. Their results show that, with the introduction of low doped region at the device surface, it is possible to manipulate the threshold voltage according to the circuit application. Also, for a given charge sheet density, the introduction of a low doped epitaxial region produces a reduction of the electron effective field, resulting in the improvement of electron effective mobility. But it leaves the total gate capacitance unaffected.

Barlage *et. al.* have used the transmission line model for the MOSFET channel region for extraction of inversion MOS capacitance [15]. His work corrects the capacitance measurement error introduced from high gate-dielectric leakage in the inversion regime. Jallepalli *et. al.* have reported a first-principle approach to inversion layer quantization which is valid for arbitrary and complex band structures [16]. They performed the self-consistent calculation for n-MOSFETs and p-MOSFETs with the QM calculation based on full band formalism. They have showed that the full band formalism though complicated, can accurately calculate the threshold voltage, V_T , shift and electrical oxide thickness. Finally, they obtained a set of constant effective masses to describe the electrical effects of quantization to first order. Using those effective masses the gate capacitance have been calculated which shows a good agreement with the available experimental data.

As mentioned earlier, one-band effective mass analysis is applied to study hole quantization, using constant effective mass derived from bulk silicon to calculate hole subband energies and threshold voltage, V_T , shift in p-MOSFET. But due to the valance band mixing, the traditional one-band effective mass approximation (EMA) using bulk effective masses may not describe the hole quantization accurately. Due to the strong band mixing effect, the dispersion of hole subband is far from parabolic and also become dependent on electric field. Recently, Hou *et. al.* have reported a model based on six-band (electric field dependent) effective mass for hole quantization [17]. They also proposed a set of constant empirical effective mass values to describe V_T shifts. In their analysis, effects of inversion charges were neglected, which implies that the model is valid only in sub-threshold and near threshold regions and not in strong inversion. They have shown that the calculated V_T shift in p-MOSFET by the improved one-band EMA using field independent empirical effective mass is well in agreement with the experimental data.

Giannini *et. al.* have compared the results of measurements of MOS interface states by capacitance-voltage (C-V) and charge pumping techniques [18]. They have shown that, if the effects of carrier tunneling in slow oxide traps are

not incorporated, the information on energy distribution of interface states given by both capacitance-voltage and charge pumping techniques will be erroneous. Pacelli *et. al.* have shown that semi-classical model is not acceptable even near flat band region [19]. It is well known that a strong surface electric field causes the confinement of carrier at the oxide interface. But the study of Pacelli shows that even for a small vertical electric field, due to the presence of abrupt discontinuity at the Si/SiO_2 , a “dark space” of a few nanometer results. In this “dark space”, the majority carrier density is much lower than in the bulk. This work shows that significant quantum effects can occur in the absence of a full confining potential.

Calculation of gate leakage current in submicron MOSFETs is another important topic of study. Rana *et. al.* used self-consistent solutions of accumulated layers in n-type substrate MOSFET to calculate the tunneling current [20]. Tunneling current from inversion layer was studied by Lo *et. al.* [21]. They showed that for the purpose of modeling tunneling characteristics of electrons, the transmission probability concept is not acceptable and the well known WKB (Wentzel-Krammer-Brioullion) approximation or the numerical integration of Airy function is not valid. They have used the transverse resonant method, applicable for electromagnetic waves in a waveguide, for solving the Schrödinger’s equation. The complex eigenenergy found from the solution of the Schrödinger’s equation is used to calculate the gate leakage current. Shih *et. al.* have compared the leakage current found from the numerical solution to that found by using WKB approximation [22]. They showed that the gate leakage current found from the WKB approximation shows poor agreement at high gate voltages. As the classical WKB approximation does not account for the wave reflections from the material interface, Yang *et. al.* have used a modified WKB approach [23]. This approach addresses interface reflection, however, replaces the traditional trapezoidal barrier with a rectangular one. The suggestion that comes from their study is that alternative dielectrics with higher dielectric constant may be used in lieu of SiO_2 to reduce the tunneling current. In order to have a greater understanding about how a dielectric stack with high-k materials would affect the direct tunneling current, Mudanai *et. al.* have performed a study [24]. It is found that the reduction

in direct tunneling current in high-k dielectrics is less than as expected as the barrier height are usually lower than that in SiO_2 .

Abramo *et. al.* have reported a QM solver for the two-dimensional (2-D) Schrödinger's equation based on the k-space representation of the solution [25]. They have applied it to simulate the 2-D electrostatic quantum effects in nano-scale MOS transistors. They have shown the presence of quantum effects of purely 2-D nature in the channel and source/drain regions of scaled ULSI MOS devices, which cannot be properly accounted for in 1-D or quasi 2-D approaches.

Schrödinger's equation has been solved in Refs. [24, 26] allowing wave function penetration into the gate dielectric for the first time. Haque *et. al.* calculated the effects of wave function penetration into gate oxide [26]. For simplicity, they have avoided the self-consistent solution and used an exponential potential profile. They have shown that the traditional boundary condition over estimates the average distance of the carriers from the interface by a few angstroms. Mudanai *et. al.* have done the self-consistent solution using the first order perturbation approach for allowing wavefunction penetration into the gate oxide and gate electrode [24]. Effects of wave function penetration on the gate capacitance has also been studied recently by Mudanai *et. al.* [27]. They have shown that accounting for wave function penetration into the gate dielectric causes the carrier profile to be shifted closer to the gate dielectric reducing the electrical oxide thickness. Due to this shift, the gate capacitance is increased in the presence of penetration and this effect is more pronounced at higher gate voltages.

1.2 Objective of the Work

Quantization effects in MOS inversion layers are typically studied by self-consistent solution of coupled Schrödinger's and Poisson's equations [3, 6]. The boundary conditions commonly used for the solution of Schrödinger's equation are that the wave function goes to zero at silicon-oxide interface and at some point deep inside the bulk [3]. The first condition is equivalent to assuming that the potential barrier height at the silicon-oxide interface seen by the inversion carriers is infin-

ity. It is known that the actual barrier height is finite, and for electrons, this is approximately equal to 3 eV. Therefore, some penetration of the wave function into the gate oxide is expected. While this penetration has negligible effects in devices with thick oxide layers, its neglect in deep submicron MOSFETs cannot be justified. Yet, in the absence of other suitable boundary conditions, zero penetration of wave function into gate oxide is assumed in the simulation of even deep submicron MOSFETs [3, 6, 7, 8, 9, 11, 12, 13, 14, 16, 18, 19, 22, 23]. In fact, in these devices, among other effects, wave function penetration is known to result in a direct tunneling gate current [20, 21].

Very little work has so far been done to understand the effects of wave function penetration on MOS device performance. Recently, calculation of the wave function including penetration into gate-oxide has been reported in the literature [24, 26]. It is found that when penetration is considered, the wave function is shifted towards the oxide by a few tenths of a nanometer, but its shape essentially remains unchanged. As a consequence, the average distance of the inversion carriers from the interface is also reduced by a few tenths of a nanometer. A reduction in the average distance of the carriers will modify the inversion layer capacitance of the devices. Effects of wave function penetration on the gate capacitance has recently been studied by Mudanai *et. al.* [27]. They have shown that due to the shift of the charge centroid, the gate capacitance increases in the presence of penetration and this effect is more pronounced at higher gate voltages. In their calculations, Mudanai *et. al.* have used a quantum transmitting boundary method [28] to include wave function penetration in the solution of Schrödinger's equation. A consequence of using this boundary condition is that the Hamiltonian becomes non-Hermitian, and complex eigenenergies of the Hamiltonian matrix are required to be determined.

When wave functions penetrate into the gate oxide, solution of Poisson's equation is affected in two ways. First, a fraction of the inversion charges reside within the oxide region. In such cases, Poisson's equation cannot be solved for only the silicon region in a self-consistent scheme without introducing errors. To account for inversion charges in oxide, Poisson's equation should be solved for the com-

bined oxide and semiconductor regions, with appropriate boundary conditions applied at the gate metal-oxide interface. Second, due to the shift of the inversion charge centroid in the presence of penetration, the band bending in silicon will be different when penetration effects are considered. This, in turn, will modify the electrostatic potential. However, in Refs. [21, 22, 23, 24], although effects of wave function penetration on tunneling current have been included, these effects on solution of Poisson's equation have been neglected. These effects on Poisson's equation have been accounted for only in Refs. [20, 27]. In Ref. [20], it has been assumed, rather arbitrarily, that the wave function vanishes at the gate metal-oxide interface and Ref. [27] has applied the numerically complicated quantum transmitting boundary method [28]. So far, the consequences of wave function penetration on solution of Poisson's equation is yet to be studied in a systematic manner.

In this study, self-consistent modeling of deep submicron n-MOSFETs for both (111) and (100) orientations of silicon and p-MOSFETs for (100) silicon are performed, taking into account the effects of wave function penetration on the solutions of both Schrödinger's and Poisson's equations. Thus, penetration effects are included inside the self-consistent loop. To make the procedure numerically efficient, Schrödinger's equation is solved using an efficient method with new, open boundary conditions allowing for wave function penetration [29]. The proposed technique, based on Green's function formalism, eliminates the need for any matrix manipulations or determination of complex eigenenergies of non-Hermitian Hamiltonians, thus saving considerable computational time. Results of self-consistent calculations are presented and compared to those when no penetration is considered. These results are used to discuss the effects of wave function penetration on modeling of device properties and on scaling of deep submicron MOSFETs. A comparison between the penetration effects in n-MOS and p-MOS devices is also made.

1.3 Organization of the Thesis

Chapter 2 discusses the theory behind this work. In this section, at first, the existing self-consistent modeling of MOS devices is described. Then a numer-

ically efficient technique based on Green's function formalism to calculate the wave function with penetration into the gate oxide is presented. Finally, the formulation of a modified self-consistent loop is given which incorporates the wave function penetration effects into the gate dielectric on both Schrödinger's and Poisson's equations. Chapter 3 deals with the results and discussions. In this chapter various results obtained for n-MOSFETs and p-MOSFETs under different conditions are reported and discussed. Concluding remarks of this work along with suggestions for future work are presented in chapter 4.

Chapter 2

Theory

In this chapter, at first, the existing self-consistent model is reviewed. It is followed by a description of a new numerically efficient technique based on Green's function formalism to solve Schrödinger's equation. Finally a modified self-consistent formulation is presented which uses the above mentioned technique to include the effects of wave function penetration into the gate oxide.

2.1 Existing Self-Consistent Analysis

The self-consistent solution of coupled Schrödinger's and Poisson's equations as proposed by Stern [3] and Moglestue [6] is presented in this section.

2.1.1 Model

The three major approximations that Stern made are:

- (i) Effective mass approximation is valid, so that the periodic lattice potential need not be taken into account explicitly.
- (ii) Envelope wavefunction vanishes at the silicon surface.
- (iii) Surface states are neglected and any charge in the oxide adjacent to the semiconductor is replaced by an equivalent electric field. A typical conduction band profile for an n-MOS is shown in Fig. 1.1.

Within the effective mass approximation, Schrödinger's equation for the wave function ψ_{0ij} for this system can be written as,

$$\left[-\frac{1}{2}\hbar^2 \nabla m^{*-1} \nabla + eV(z) \right] \psi_{0ij} = E'_{ij} \psi_{0ij}, \quad (2.1)$$

where m^{*-1} represents the effective mass tensor, $V(z)$ the electrostatic potential, e the magnitude of the electronic charge and E'_{ij} is the energy. z is reckoned positive into the semiconductor. Following Stern [3], the electronic wavefunction ψ_{0ij} for the j th subband in the i th valley can be expressed in terms of Bloch waves traveling parallel to the interface, constrained by an envelope function normal to it, thus:

$$\psi_{0ij}(x, y, z) = \psi_{ij}(z)e^{i\theta z} e^{ik_x x + ik_y y}, \quad (2.2)$$

here, k_x and k_y represent the transverse components of the wave vector k of the electron measured relative to the band edge. θ depends on k_x and k_y . Envelope function $\psi_{ij}(z)$ is the solution of

$$\left[-\frac{\hbar^2}{2m_{zi}} \frac{d^2}{dz^2} + eV(z) \right] \psi_{ij}(z) = E_{ij} \psi_{ij}(z), \quad (2.3)$$

where, m_{zi} is the effective mass perpendicular to the interface and E_{ij} is the eigenenergies of the j th subband in the i th valley in the same direction. Boundary conditions commonly used for the solution of Eq. (2.3) are $\psi_{ij}(\infty) = 0$ deep inside the semiconductor and at the oxide-semiconductor interface, $\psi_{ij}(0) = 0$. Each eigenvalue E_{ij} found from the solution of Eq. (2.3) is the bottom of a continuum of levels called a subband, with energy levels given by the relationship,

$$E'_{ij} = E_{ij} + \hbar^2 k_x^2 / 2m_x + \hbar^2 k_y^2 / 2m_y, \quad (2.4)$$

here m_x and m_y are the principle effective masses for motion parallel to the surface. There can be as many as three values of m_z depending on the surface orientation because the conduction band of silicon has six ellipsoidal valleys along the $\langle 100 \rangle$ direction of the Brillouin zone. In the effective mass approximation, the valleys are degenerate in pairs. Thus, solution of Eq. (2.3) gives the eigenenergy E_{ij} and the envelope function $\psi_{ij}(z)$.

The potential $V(z)$ is found from the solution of Poisson's equation,

$$\frac{d^2 V(z)}{dz^2} = -\frac{[\rho_{depl}(z) - e \sum_{ij} N_{ij} |\psi_{ij}(z)|^2]}{\epsilon_{si} \epsilon_0}, \quad (2.5)$$

where, ϵ_{si} is the dielectric constant of the semiconductor, N_{ij} is the carrier concentration in the j th subband in the i th valley. N_{ij} is given by the following equation,

$$N_{ij} = \frac{n_{vi} m_{di} kT}{\pi \hbar^2} \ln \left[1 + \exp \left(\frac{E_F - E_{ij}}{kT} \right) \right], \quad (2.6)$$

where, n_{vi} is the valley degeneracy and m_{di} is the density-of-states effective mass of the i th valley, given by $m_{di} = \sqrt{m_{xi}m_{yi}}$. E_F is the Fermi energy.

$\rho_{depl}(z)$ is the charge density in the depletion layer, which is taken to be,

$$\begin{aligned}\rho_{depl}(z) &= -e(N_A - N_D), & 0 < z < z_d, \\ &= 0, & z > z_d,\end{aligned}\quad (2.7)$$

here, z_d is the depletion layer thickness given by

$$z_d = \sqrt{\frac{2\epsilon_{si}\epsilon_0\Phi_d}{e(N_A - N_D)}}, \quad (2.8)$$

where Φ_d is the band bending due to depletion charge only. Φ_d can be calculated from the following equation,

$$\Phi_d = \Phi_s - \frac{kT}{e} - \frac{eN_{inv}z_{avg}}{\epsilon_{si}\epsilon_0}. \quad (2.9)$$

Here, Φ_s is the total band bending, N_{inv} is the total number of charges per unit area in the inversion layer given by,

$$N_{inv} = \sum_{ij} N_{ij}, \quad (2.10)$$

and z_{avg} is the average penetration of inversion charge density into silicon given by,

$$z_{avg} = (1/N_{inv}) \sum_{ij} N_{ij} \int z |\psi_{ij}|^2 dz. \quad (2.11)$$

The two boundary conditions for solution of Eq. (2.5) are $\frac{dV}{dz} = 0$ for large z and at the surface, it's value is $-F_S$, where,

$$F_S = \frac{e(N_{inv} + N_{depl})}{\epsilon_{si}\epsilon_0}, \quad (2.12)$$

is the surface electric field in silicon, and

$$N_{depl} = z_d(N_A - N_D), \quad (2.13)$$

is the number of charge per unit area in the depletion layer.

2.1.2 Calculation

The self-consistent calculation starts with an initial estimate for the potential, $V(z)$ and then solves Eqs. (2.3) and (2.5) iteratively until the output potential from Eq. (2.5) agrees with the input potential in Eq. (2.3) within the specified limits.

The simplest approximation for the trial potential is to replace the potential $V(z)$ in Eq. (2.3) by $-F_S z$ for $z > 0$ and by an infinite barrier for $z < 0$. This is called triangular potential approximation. The solution of Eq. (2.3) for ψ_{ij} and E_{ij} with this approximation is given in Ref. [3]. But this approximation is reasonable only when there is a small or no charge in the inversion layer.

When all the carriers are at the lowest subband, the trial potential can be obtained by the variational approximation. For this approximation, the trial eigenenergies for the initial solutions of Eq. (2.3) are obtained by an approximate formula using the variational technique and are described in Ref. [3]. This trial potential generally leads to good convergence except at high temperature, for which the assumption that all the carriers are in the lowest subband is particularly poor. At high temperature, one should start with small values of N_{inv} and then gradually go to the larger values, taking the results of each case to construct the starting potential for the next. After solving Eq. (2.3) for ψ_{ij} and E_{ij} with the approximate equation, the Fermi energy, E_F can be found from Eq. (2.6) and (2.10) for a given N_{inv} . Once the Fermi energy is known, N_{ij} for each subband can be calculated from Eq. (2.6).

The potential $V(z)$ is determined by solving the Poisson's equation Eq. (2.5) using the boundary conditions described above. The potential thus obtained is inserted for $V(z)$ in Schrödinger's equation, which is re-solved in the manner just described. New values for E_F and E_{ij} for all subbands under consideration are re-estimated using the equations already given. Poisson's equation can be solved again and this procedure is repeated until the potential distribution and energies converge.

The convergence criteria are that successive eigenvalues in the solution of the Schrödinger equation (Eq. (2.3)) with a given potential agree to within 10^{-6} eV and that the potentials in successive rounds of iteration differ by no more than the larger of $KT/2000$, $(E_F - E_0)/10^4$, or 10^{-6} eV. Another important criteria for the convergence is the convergence of E_F because it is the most sensitive to the change of ψ and V .

2.2 Green's Function Formalism

The Green's function is a powerful concept that gives us the response at any point due to an excitation at any other. For the MOS inversion layer, retarded Green's function for the i th valley at any distance z is defined by the relationship,

$$\left[E + \frac{\hbar^2}{2m_{zi}} \frac{\partial^2}{\partial z^2} - eV(z) + i\epsilon \right] G_i^R(z, z'; E) = \delta(z - z'), \quad (2.14)$$

where ϵ is an infinitesimally small positive energy. The retarded Green's function, $G_i^R(z, z'; E)$, can be viewed as the wave function at z resulting from a unit excitation applied at z' . According to the nature of Green's function, it is continuous at $z = z'$ but its derivative is discontinuous by, $2m_{zi}/\hbar^2$ at z' .

G_i^R is used to calculate the one-dimensional density-of-states, N_{1D} , eigenenergies, E_{ij} and normalized wavefunctions, ψ_{ij} . The logarithmic derivative of the retarded Green's function G^R is defined by [30]:

$$Z_i(z, z'; E) = \frac{2\hbar}{im_{zi}} \left[\frac{\partial G_i^R(z, z'; E)}{\partial z} / G_i^R(z, z'; E) \right]. \quad (2.15)$$

Since $Z_i(z, z'; E)$ has a discontinuity at $z = z'$, one needs two boundary conditions. To obtain these conditions, it is assumed that the potential is flat sufficiently far from the oxide-silicon interface in both directions. Let $V(-\infty)$ is the value of constant potential deep inside the gate-metal and $V(\infty)$ is the value of constant potential deep inside the bulk silicon. Green's function in those regions may be expressed as,

$$G_i^R(z \rightarrow \infty, z'; E) \sim e^{\gamma_i(\infty)(z-z')}, \quad (2.16)$$

and

$$G_i^R(z \rightarrow -\infty, z'; E) \sim e^{-\gamma_i(-\infty)(z-z')}, \quad (2.17)$$

where $\gamma_i(\pm\infty) = i\sqrt{(2m_{zi}/\hbar^2)(E - eV(\pm\infty) + i\epsilon)}$. The boundary conditions to calculate Z_i are determined from Eqs. (2.16) and (2.17). These are,

$$Z_i(z \rightarrow \infty, z'; E) = Z_{oi}(\infty), z > z', \quad (2.18)$$

and

$$Z_i(z \rightarrow -\infty, z'; E) = -Z_{oi}(-\infty), z < z', \quad (2.19)$$

where $Z_{oi}(\pm\infty) = (2\hbar/im_{zi})\gamma_i(\pm\infty)$. From the properties of 1D Green's functions, it can be shown [30] that, for all $z > z'$:

$$Z_i(z, z'; E) = Z_i^+(z; E), \quad (2.20)$$

and for all $z < z'$:

$$Z_i(z, z'; E) = Z_i^-(z; E). \quad (2.21)$$

Note that $Z_i^+(Z_i^-)$ does not depend on z' as long as $z > z'(z < z')$. The method for calculating Z_i^\pm have been discussed in detail in Ref. [31]. Z_i^\pm are calculated using a method analogous to the impedance transformation technique of microwave transmission lines along with the two boundary conditions given in Eqs. (2.18) and (2.19).

The normalized wave function can be obtained from retarded Green's function. From the well known expansion of G_i^R in terms of the complete set of eigenfunctions:

$$G_i^R(z, z'; E) = \sum_j \frac{\psi_{ij}(z)\psi_{ij}^*(z')}{E - E_{ij} + i\epsilon}, \quad (2.22)$$

If $E_{i(j+1)} - E_{ij} \gg \epsilon$ for all values of j , only one term in the series dominates when $E \rightarrow E_{ij}$, since the discrete eigenenergies in one-dimension are nondegenerate. For the diagonal elements of G_i^R , we obtain

$$G_i^R(z, z; E \rightarrow E_{ij}) \cong \frac{|\psi_{ij}(z)|^2}{E - E_{ij} + i\epsilon}, \quad (2.23)$$

Taking imaginary parts of both sides of Eq. (2.23) and substituting $E = E_{ij}$,

$$|\psi_{ij}(z)|^2 = -\epsilon \Im [G_i^R(z, z'; E_{ij})]. \quad (2.24)$$

It has been shown in Ref. [30] that,

$$-\Im [G_i^R(z, z'; E)] = \frac{4}{\hbar} \Im \left(\frac{i}{Z_i^+(z; E_{ij}) - Z_i^-(z; E_{ij})} \right), \quad (2.25)$$

Substituting Eq.(2.25) in Eq.(2.24),

$$|\psi_{ij}(z)|^2 = \frac{4\epsilon}{\hbar} \Im m \left(\frac{i}{Z_i^+(z; E_{ij}) - Z_i^-(z; E_{ij})} \right). \quad (2.26)$$

The 1D density-of-states, N_{1D} , is related to the diagonal part of G^R . $N_{1D_i}(z; E)$, in terms of retarded Green's function, G_i^R is given by,

$$N_{1D_i}(z; E) = -\frac{1}{\pi} \Im m \left[G_i^R(z, z'; E) \right], \quad (2.27)$$

As $\epsilon \rightarrow 0^+$, the density-of-states (DOS), $N_{1D_i}(z; E)$, becomes delta functions at the eigenenergies, $E = E_{ij}$ in a bound system with the amplitude equal to the probability density at that energy, *i.e.*,

$$N_{1D_i}(z; E) = \sum_j |\psi_{ij}(z)|^2 \delta(E - E_{ij}). \quad (2.28)$$

In the presence of inelastic scattering or in a leaky quantum well, G_i^R is defined by Eq. (2.14) with ϵ replaced by V_i . Here $V_i = \hbar/2\tau_i$ where τ_i is the phase-breaking time in the presence of inelastic scattering and is the carrier life time in the quantum well in case of a leaky well. When E approaches E_{ij} , the density-of-states is given by the familiar Lorentzian shape:

$$N_{1D_i}(z; E) = \frac{V_i}{\pi} \frac{|\psi_{ij}(z)|^2}{(E - E_{ij})^2 + V_i^2}, \quad (2.29)$$

Using the definition in Eq. (2.27), N_{1D} can be expressed in terms of the logarithmic derivative Z_i^\pm [29]:

$$N_{1D_i}(z; E) = \frac{4}{\pi\hbar} \Im m \left(\frac{i}{Z^+(z; E) - Z^-(z; E)} \right). \quad (2.30)$$

The eigenenergies of a quasi-bound state, E_{ij} can easily be found by locating the peaks of N_{1D_i} , evaluated using Eq. (2.30). Once the eigenenergies have been found, the normalized wave functions can be calculated using Eq. (2.26).

2.3 Modification of Self-Consistent Analysis in the Presence of Wave Function Penetration

Properties of carriers in MOS inversion layers are studied by solving coupled Schrödinger's and Poisson's equations self-consistently. Within the effective-mass

approximation, the 3D Schrödinger's equation in a MOS inversion layer may be decoupled into a 1D equation that describes the envelope function in the direction normal to the interface. For a parabolic bandstructure, 1D Schrödinger's equation is given by Eq. (2.3). When the traditional boundary conditions are used, the effects of wave function penetration are neglected. In order to include wave function penetration, an open boundary condition is required to be applied at silicon-oxide interface that should take into account the quasi-bound nature of the inversion layer states.

In this study, we use a new technique presented in Section 2.2. As already indicated, open boundary conditions are used which are based on the assumption that the potential profile is flat at deep inside the gate metal as well as at deep inside the bulk semiconductor. This assumption implies that the wave function deep inside the semiconductor is exponentially decaying ($E < eV(\infty)$) and deep inside the gate metal, the wave function is a plane wave ($E > eV(-\infty)$).

Since a fraction of inversion charge resides within the gate oxide due to wave function penetration, Poisson's equation should be solved for the combined oxide and semiconductor regions. Considering wave function penetration, Poisson's equation is written as

$$\begin{aligned} d^2V(z)/dz^2 &= -\rho_{inv}(z)/\epsilon_0\epsilon_{ox}, & -T_{ox} < z < 0, \\ &= -[\rho_{depl}(z) + \rho_{inv}(z)]/\epsilon_0\epsilon_{Si}, & z > 0, \end{aligned} \quad (2.31)$$

where

$$\rho_{inv}(z) = -e \sum_{ij} N_{ij} |\psi_{ij}(z)|^2, \quad (2.32)$$

and $\rho_{depl}(z)$ is defined by Eq. (2.7). In Eq. (2.32), N_{ij} is given by Eq. (2.6). When $|\psi_{ij}(z)|^2$, calculated with penetration, is used to define ρ_{inv} in Eq. (2.32), effects of shift of inversion charges on the solution of Poisson's equation are also included.

The boundary conditions required to solve Eq. (2.31) can no longer be applied at the semiconductor-oxide interface [3] due to the presence of inversion charges in the oxide. Instead, the boundary conditions used are that dV/dz vanishes for large z and that its value at the gate metal-oxide interface ($z = -T_{ox}$) be $-F_{ox}$,

where

$$F_{ox} = e(N_{inv} + N_{depl}) / \epsilon_0 \epsilon_{ox}, \quad (2.33)$$

N_{inv} and N_{depl} are given by Eqs. (2.10) and (2.13), respectively. Eq. (2.33) assumes that the wave function tail in the gate oxide region has decayed to an insignificant value at $z = -T_{ox}$. This assumption has been found to be valid in devices with $T_{ox} \geq 0.5$ nm [27]. Another relationship necessary to relate oxide field F_{ox} to silicon field F_s at $z = 0$ is that $\epsilon_{ox} F_{ox} = \epsilon_{Si} F_s$.

Under the modified self-consistent analysis, Eqs. (2.3) and (2.31) - (2.33) are solved iteratively. The calculation should be started with small values of N_{inv} and then gradually go to the larger values, taking the results of each case to construct the starting potential for the next. The initial potential $V(z)$ is obtained by solving Poisson's equation assuming $N_{inv} = 0$. For a given potential $V(z)$, the eigenenergies of the quasi-bound states, E_{ij} , are calculated by locating the peaks of N_{1D_i} where the 1D DOS, N_{1D} , is calculated using Eq. (2.30). The logarithmic derivative, Z_i^\pm can be calculated as functions of z using Eqs. (2.18) and (2.19) [31]. The corresponding wave functions including penetration into the gate dielectric can then easily be obtained from the relationship mentioned in Eq. (2.26). Once Eq. (2.3) is solved for E_{ij} and ψ_{ij} , taking into account the effects of wave function penetration, the Fermi energy, E_F can be found from Eq. (2.6) and (2.10) for a given N_{inv} . Once the Fermi energy is known, N_{ij} for each subband can be calculated from Eq. (2.6). The potential $V(z)$ is determined by solving the Poisson's equation Eq. (2.31) and (2.32) using the boundary conditions described in Eq. (2.33). The potential thus obtained is inserted for $V(z)$ in Schrödinger's equation, which is re-solved in the manner just described. New values for E_F and E_{ij} for all subbands under consideration are re-estimated using the equations already given. Poisson's equation can be solved again and this procedure is repeated until the potential distribution and energies converge.

As a convergence criteria, percent changes in Fermi energy, E_F and the first eigenenergy E_{i1} of the new iteration are compared to those of the previous iteration and the self-consistent loop is terminated when a accuracy of 0.05% or less is reached. A flow chart of our algorithm is given in Appendix A.

Chapter 3

Results and Discussions

The results of the self-consistent calculation for MOS devices considering the effects of wavefunction penetration are presented in this Chapter. The self-consistent calculations for n-MOSFETs have been performed for two different orientations of silicon, $\langle 111 \rangle$ and $\langle 100 \rangle$. Calculations have also been done for p-MOSFET on $\langle 100 \rangle$ silicon to compare the effects of penetration on electrons and holes.

3.1 Effective mass approximation

In MOS devices, for the chosen interface that lies in the (100) crystal planes, the effective mass tensor becomes diagonal in the co-ordinate system which has its z -axis perpendicular to the surface pointing into the semiconductor. It is known that silicon has six ellipsoidal constant energy surfaces in the conduction band. The $\langle 111 \rangle$ surfaces have only one ladder of subbands with degeneracy 6 in the direction normal to the interface, since all the valleys have the same orientation with respect to the surface. For the $\langle 100 \rangle$ oriented surfaces, m_z for electrons can take the value of the longitudinal effective mass, m_l , for the two bulk constant energy ellipsoid perpendicular to the surface giving rise to a two-fold degenerate subband ladder and the value of the transverse effective mass, m_t , for the other four ellipsoids, giving rise to a four-fold degenerate ladder. The valleys which present the higher effective mass perpendicular to the surface have the lowest kinetic energy and lowest energy levels. Effective mass approximation has been found to be accurate in describing the quantization effects of electrons in a MOS

inversion layer [16]. The values of different parameters used in the calculation are taken from Ref. [3] and are summarized in Table 3.1.

Surface	(111)	(100)	
Valleys	All	m_l	m_t
Degeneracy, n_v	6	2	4
Normal mass, m_z/m_0	0.258	0.916	0.190
Density of state mass, m_d/m_0	0.358	0.190	0.417

Table 3.1: Effective masses of electrons in different valleys.

It is known that the energy band structure for holes is non-parabolic. So, it is questionable to represent the valance band within the effective mass approximation. A first principle formalism has been used to completely describe the valance band structure including the periodic lattice potential [16]. But this technique is very complicated and is numerically inefficient. On the other hand, bulk effective mass approximation has been found to be accurate in describing the inversion layer capacitance for holes [12]. Recently, Ref. [17] showed that the effective mass of the inversion layer holes are different from that of the bulk near threshold region. But this analysis neglects inversion charge, and as a result, is not valid in strong inversion. For these reasons, in this study, we also use the bulk effective mass approximation of Refs. [6, 12].

The constant-energy surfaces of the light hole and the heavy hole bands are represented by,

$$E_h = \left(\frac{\hbar^2 k^2}{2m_0} \right) \left[A \mp \left(B^2 + C^2 \left(\frac{k_x^2 k_y^2 + k_y^2 k_z^2 + k_z^2 k_x^2}{k^4} \right) \right)^{1/2} \right] \quad (3.1)$$

and is reckoned positive downwards into the valance band. Here, + and - corresponds to the light hole and heavy hole bands, respectively. The parameters A, B, C are physical constants which are determined experimentally in Ref. [6].

For the split-off band holes, the constant energy surfaces are isotropic and centered around Γ (zone center). With the three types of hole bands, we get three energy ladders. In the bulk, the light and heavy hole bands are degenerate at the Γ point (valance band edge), while the third one is separated from the

other two by $\Delta E = 44$ meV due to spin-orbit coupling.

The effective mass perpendicular to Si/SiO_2 interface, m_z and density-of-states effective mass, m_d at the valance band edge on a (100) surface are reported in Refs. [6, 12]. The values of the effective masses for holes in (100) silicon used in this study are listed in Table 3.2.

	m_z/m_0	m_d/m_0
Heavy hole	0.29	0.433
Light hole	0.20	0.169
Split-off hole	0.29	0.433

Table 3.2: Effective masses for different types of holes.

3.2 n-MOS Devices on (111) silicon

Self-consistent calculations for n-MOS devices on (111) silicon are presented in this section. All the results are calculated at room temperature. Values of different parameters for silicon are taken from Ref. [3] and Table-3.1. The potential barrier height at silicon-oxide interface is considered to be 3.1 eV. Electron effective mass in oxide is assumed to be $0.5 m_0$ with a parabolic dispersion relationship. Aluminum is considered as the gate electrode with a work function equal to 4.1 eV. Our numerical calculations have shown that the effects of wave function penetration on F_s obtained from the solution of Poisson's equation due to presence of charges in oxide layer is around 1 % at strong inversion. Influences of this change in F_s on E_{ij} are non-trivial.

Fig. 3.1 shows $\rho_{inv}(z)$ as a function of z calculated using both boundary conditions. The doping density $N_A = 5 \times 10^{17} \text{ cm}^{-3}$, the oxide thickness $T_{ox} = 1.5$ nm and the calculation is for an inversion carrier density $N_{inv} = 10^{13} \text{ cm}^{-2}$. As expected, the charge density profiles calculated with both boundary conditions are essentially similar, but the distribution calculated with penetration is shifted towards the oxide by a few tenths of a nanometer [26, 27].

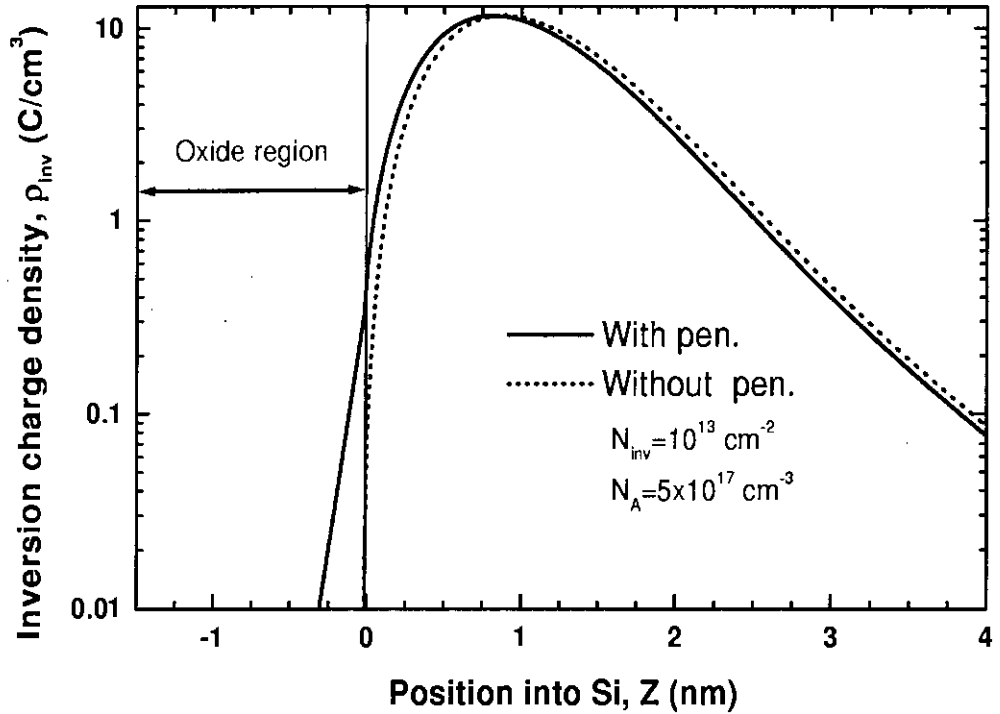


Fig. 3.1: Local inversion charge density, ρ_{inv} , as a function of position into silicon, z , calculated with and without considering wave function penetration. Doping density $N_A = 5 \times 10^{17} \text{ cm}^{-3}$ and oxide thickness $T_{ox} = 1.5 \text{ nm}$. Calculations are performed for an inversion sheet density $N_{inv} = 10^{13} \text{ cm}^{-2}$.

Fig. 3.2 is the plot of the average distance z_{avg} of the inversion electrons from the interface as a function of inversion carrier density, N_{inv} . z_{avg} is given by Eq. 2.11. Here, the doping density and the oxide thickness are the same as those used in Fig. 3.1. z_{avg} is weakly dependent on N_{inv} in weak inversion regime, but decreases sharply with increasing inversion charge density in strong inversion. It is observed that when penetration is not considered, z_{avg} is over-estimated by about 0.25 nm, and this difference is insensitive to inversion charge density (or gate voltage). It is reported in Ref. [27] that the shift in peak increases with increasing gate voltage. However, Fig. 3.2 shows that gate voltage (or inversion charge density) has little effect on the amount of shift in average distance of carriers from the interface. Δz_{avg} , the relative difference between z_{avg} calculated

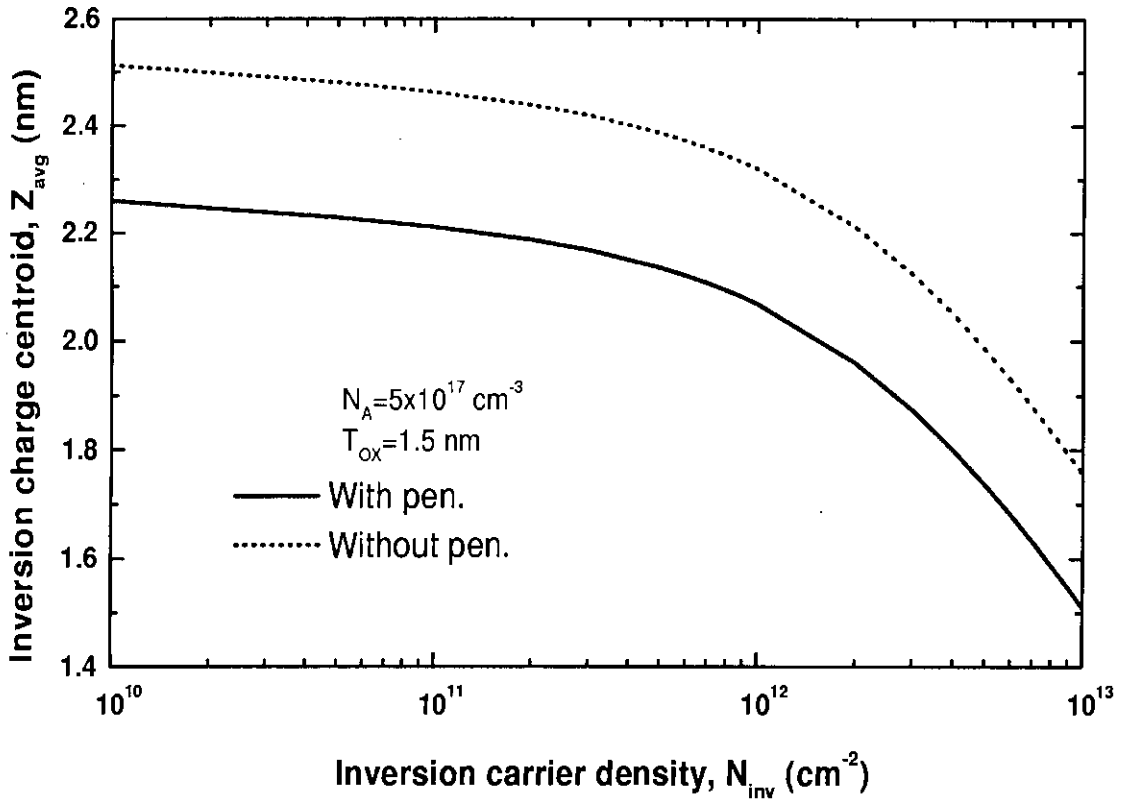


Fig. 3.2: Average distance of the inversion carriers from the interface, z_{avg} vs N_{inv} . $N_A = 5 \times 10^{17} \text{ cm}^{-3}$ and $T_{ox} = 1.5 \text{ nm}$.

using both boundary conditions is shown in Fig. 3.3. Since the value of the shift in z_{avg} remains constant, its relative error increases with increasing N_{inv} due to decrease in z_{avg} . We have calculated Δz_{avg} for three different oxide thickness and for two different doping densities. For a given doping density, Δz_{avg} is found to be independent of oxide thickness. On the other hand, the magnitude of the relative error increases with increasing doping density. Results show that the relative error in estimating z_{avg} is significant over the entire inversion region for all values of oxide thickness and doping densities considered.

Next, we study the effects of penetration on band bending. Band bending ϕ_s consists of two components: $\phi_s = \phi_d + \phi_I$, where ϕ_d is the band bending due to depletion charges and ϕ_I is the band bending due to inversion charges. Since band bending is obtained from the solution of Poisson's equation, in or-

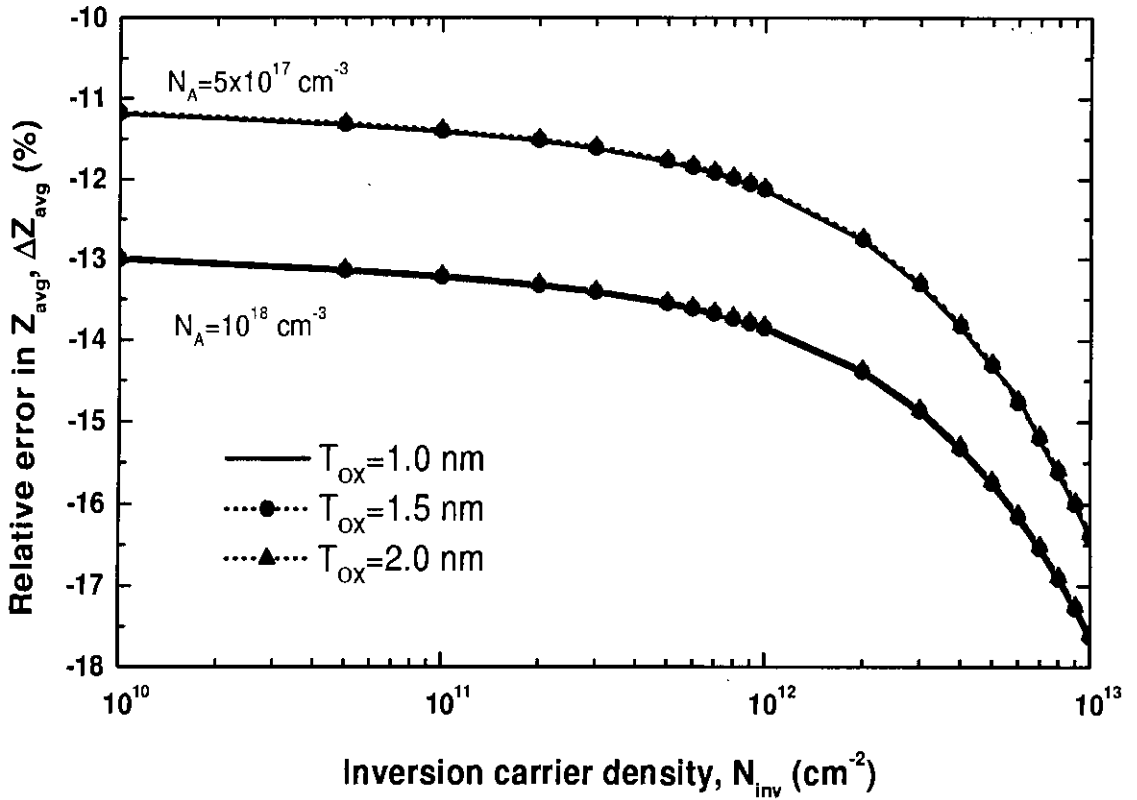


Fig. 3.3: Relative error in z_{avg} , Δz_{avg} , as a function of N_{inv} . Calculations are for three oxide widths, $T_{ox}=1.0$ nm, 1.5 nm, 2.0 nm, and two doping densities, $N_A = 5 \times 10^{17} \text{ cm}^{-3}$ and 10^{18} cm^{-3} .

der to study this effect, it is essential that effects of wave function penetration are incorporated within the self-consistent loop. Our numerical calculation has demonstrated that wave function penetration into the gate oxide has no effect on ϕ_d . Fig. 3.4 shows ϕ_I as a function of N_{inv} for the same values of doping density and gate oxide thickness as used in Fig. 3.1. ϕ_I calculated with penetration is lower than that calculated without penetration and the difference between the two increases as the inversion grows stronger. This can be explained in terms of lower z_{avg} when penetration is considered and in terms of increasing error, Δz_{avg} with increasing N_{inv} . Fig. 3.5 is the plot of $\Delta\phi_I$, the relative error in ϕ_I . It is seen that $\Delta\phi_I$, too, is independent of oxide thickness and the magnitude of the relative error increases with increasing doping density. The magnitude and the variation of $\Delta\phi_I$ in Fig. 3.5 is found to be identical to that of Δz_{avg} (Fig. 3.3).

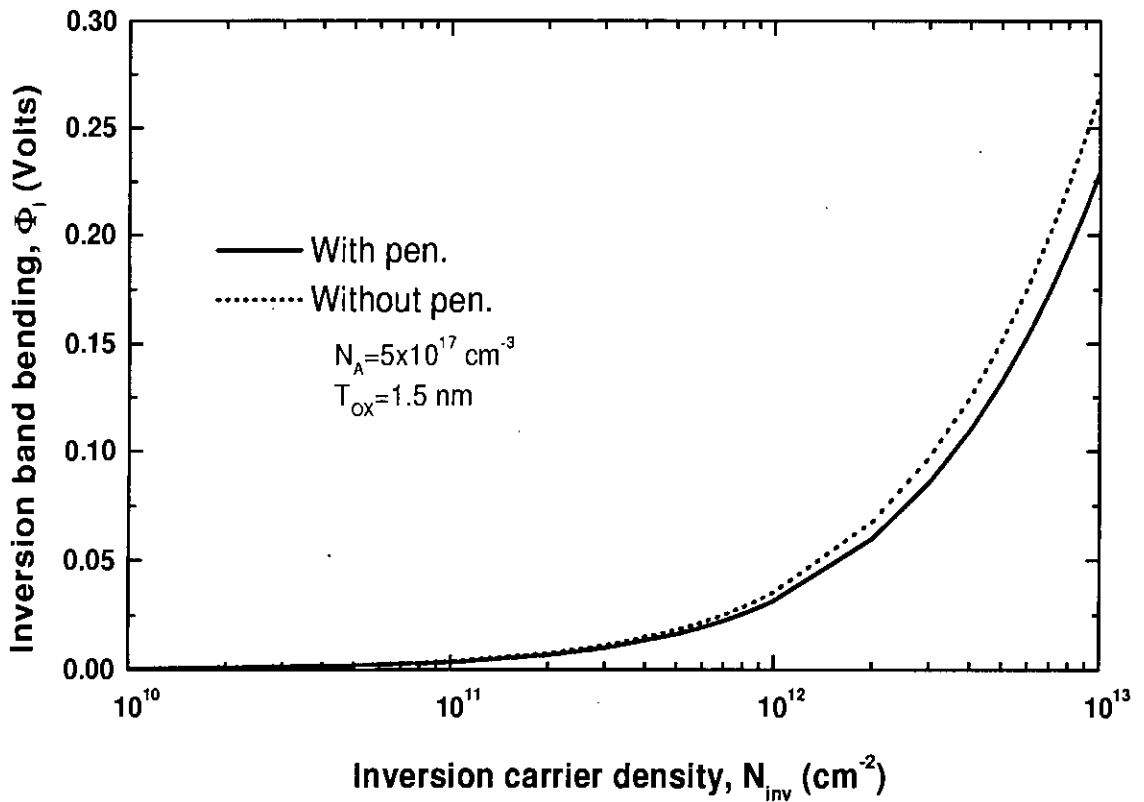


Fig. 3.4: Band bending ϕ_I due to inversion charge as a function of N_{inv} . $N_A = 5 \times 10^{17} \text{ cm}^{-3}$ and $T_{ox} = 1.5 \text{ nm}$.

This is due to the fact that in a given device for a certain N_{inv} , ϕ_I is proportional to z_{avg} .

Another important quantity that has significant effects on MOS properties is the inversion capacitance C_{inv} , defined as $C_{inv} = e \partial N_{inv} / \partial \phi_s$ [13]. The gate capacitance C_g of a MOSFET is expressed as a series combination of the oxide capacitance C_{ox} and C_{inv} , i. e., $C_g = C_{ox} / (1 + C_{ox} / C_{inv})$. Fig. 3.6 shows C_{inv} as a function of N_{inv} calculated using both the boundary conditions. Since z_{avg} with penetration is smaller, C_{inv} is higher when penetration effects are considered. Fig. 3.7 is the plot of ΔC_{inv} , the relative error in C_{inv} . Again, we find that oxide thickness has no effect on calculation of C_{inv} and the relative error slightly increases with increasing doping density.

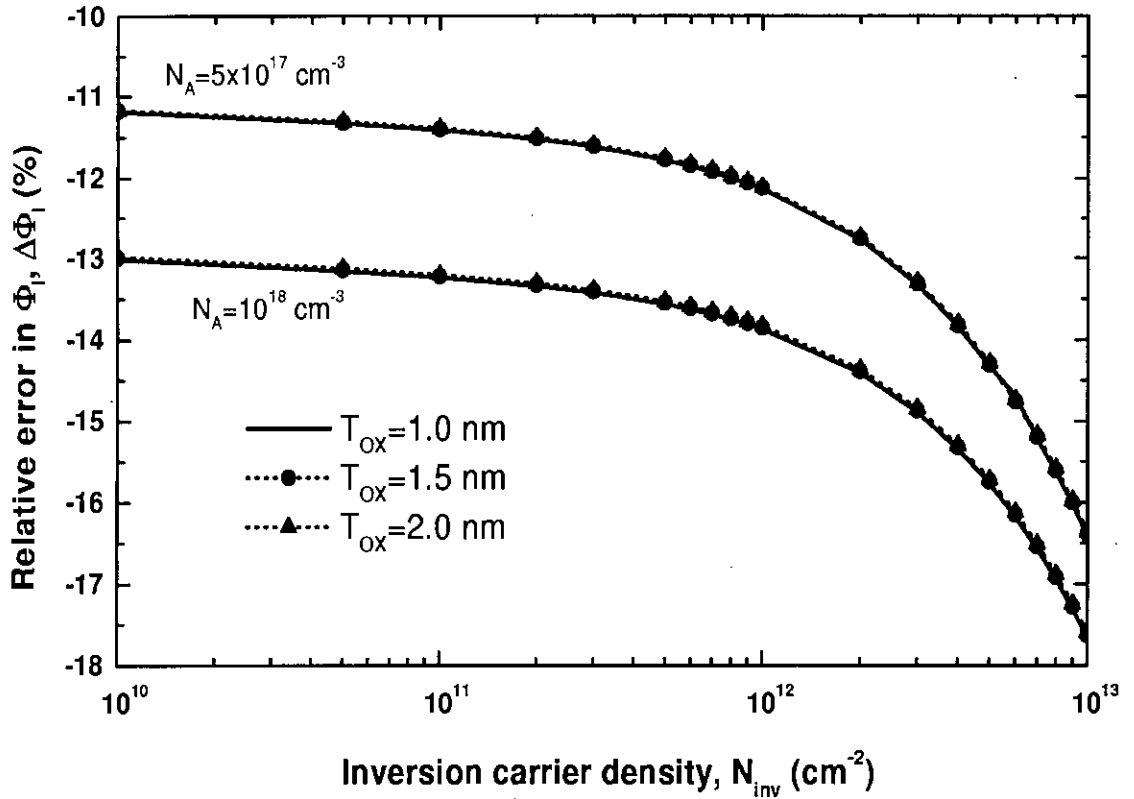


Fig. 3.5: Relative error in ϕ_I , $\Delta\phi_I$ vs N_{inv} for $T_{ox} = 1.0$ nm, 1.5 nm, 2.0 nm and $N_A = 5 \times 10^{17} \text{ cm}^{-3}$ and 10^{18} cm^{-3} .

Fig. 3.8 is the plot of gate capacitance, C_g , as a function of V_g for both with penetration and without penetration conditions. Here C_g is calculated from the basic definition that $C_g = e\partial N_{tot}/\partial V_g$, where $N_{tot} = N_{dep} + N_{inv}$, and no additional approximation has been invoked. Here gate voltage, V_g is given by, $V_g = \phi_{ms} + T_{ox}F_{ox} + \phi_s$, where ϕ_{ms} is the work function difference between gate metal and silicon. The slight non-monotonic nature of C_g is due to numerical differentiation and has no physical significance. Because C_{inv} is higher when penetration is considered, C_g with penetration is higher. Fig. 3.9 is the plot of relative error in gate capacitance, ΔC_g , as a function of V_g . It is already known that due to finite C_{inv} (non-zero z_{avg}), gate capacitance is attenuated in deep submicron MOSFETs. Our results indicate that the degradation of C_g is over-estimated when penetration effects are not considered. This over-estimation is more severe at higher gate voltages as ΔC_{inv} higher in that region. The relative error in C_g ,

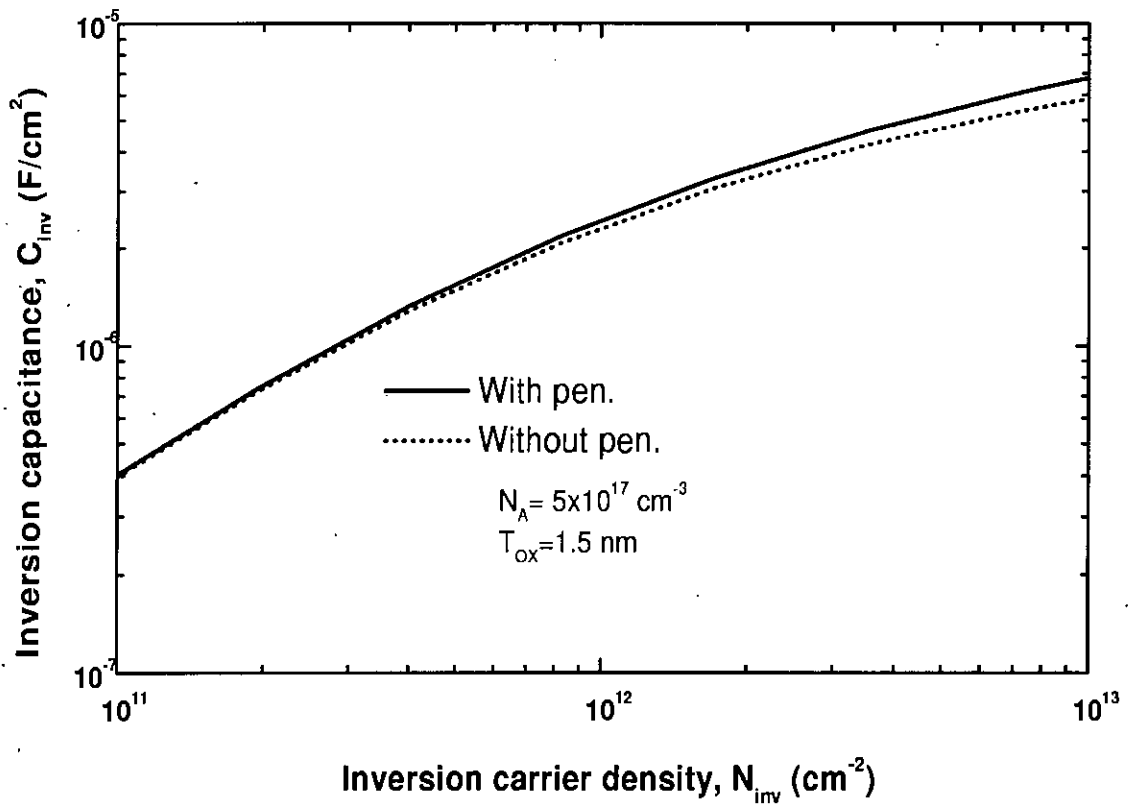


Fig. 3.6: Inversion capacitance C_{inv} vs N_{inv} for $N_A = 5 \times 10^{17} \text{ cm}^{-3}$ and $T_{ox} = 1.5 \text{ nm}$.

ΔC_g is small in the sub-threshold region and increases sharply near threshold. In strong inversion, the error is greater than 5% and is weakly dependent on V_g .

Finally, the effects of wave function penetration on threshold voltage, V_{TH} , and supply voltage, V_{DD} , of scaled MOSFETs are investigated. It has been shown in Ref. [13] that a finite value of C_{inv} leads to higher value of gate voltage required to induce a certain inversion carrier concentration in the channel. Following Ref. [13], V_{TH} , and V_{DD} are defined as the gate voltages necessary to induce an N_{inv} equal to 10^{11} cm^{-2} and $7 \times 10^{12} \text{ cm}^{-2}$, respectively. Fig. 3.10 shows relative errors in threshold voltage, ΔV_{TH} and in supply voltage ΔV_{DD} as functions of doping density N_A for different values of oxide thickness. These errors are contributed mostly by the error in estimating ϕ_I (Figs. 3.4 and 3.5). It is seen that wave function penetration effects on threshold voltage is important only in devices with

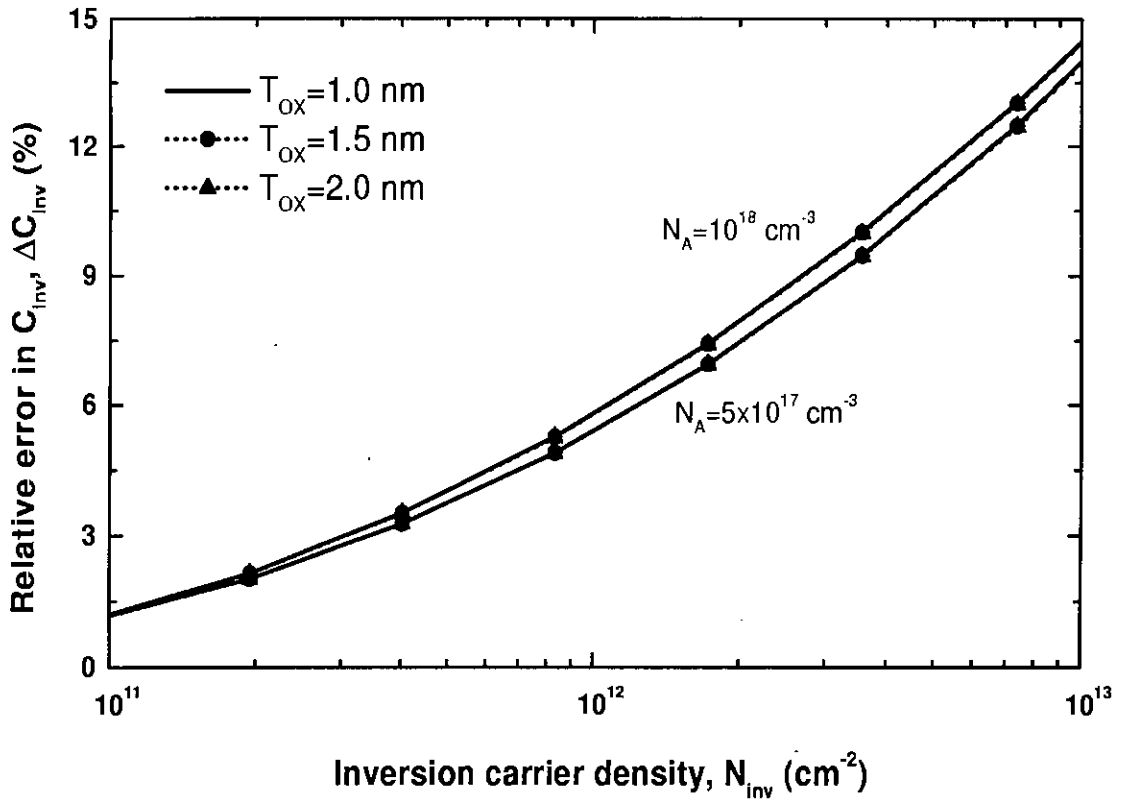


Fig. 3.7: Relative error in C_{inv} , ΔC_{inv} , as a function of N_{inv} for $T_{ox} = 1.0$ nm, 1.5 nm, 2.0 nm and $N_A = 5 \times 10^{17} \text{ cm}^{-3}$ and 10^{18} cm^{-3} .

low substrate doping and thin gate-oxides. However, since this condition is not usually realized in practical devices, penetration effects on threshold voltage of real devices are said to be insignificant. As the inversion carrier density is small at threshold, the band bending at threshold is mainly due to depletion charges, and we have already seen that this is not influenced by penetration effects. On the other hand, the relative error in estimating V_{DD} can be as high as a few percent. In Fig. 3.10, decreasing oxide thickness increases the magnitude of ΔV_{DD} and increasing doping density decreases the magnitude of ΔV_{DD} . The reasons for these two opposite trends can be explained with the help of the following arguments. When the oxide thickness is reduced, gate voltage for a given N_{inv} also reduces and the same percentage error in calculating ϕ_I constitutes a greater fraction of the total gate voltage and the error in V_{DD} increases. On the other hand, when doping density increases, ϕ_d required to reach strong inversion also

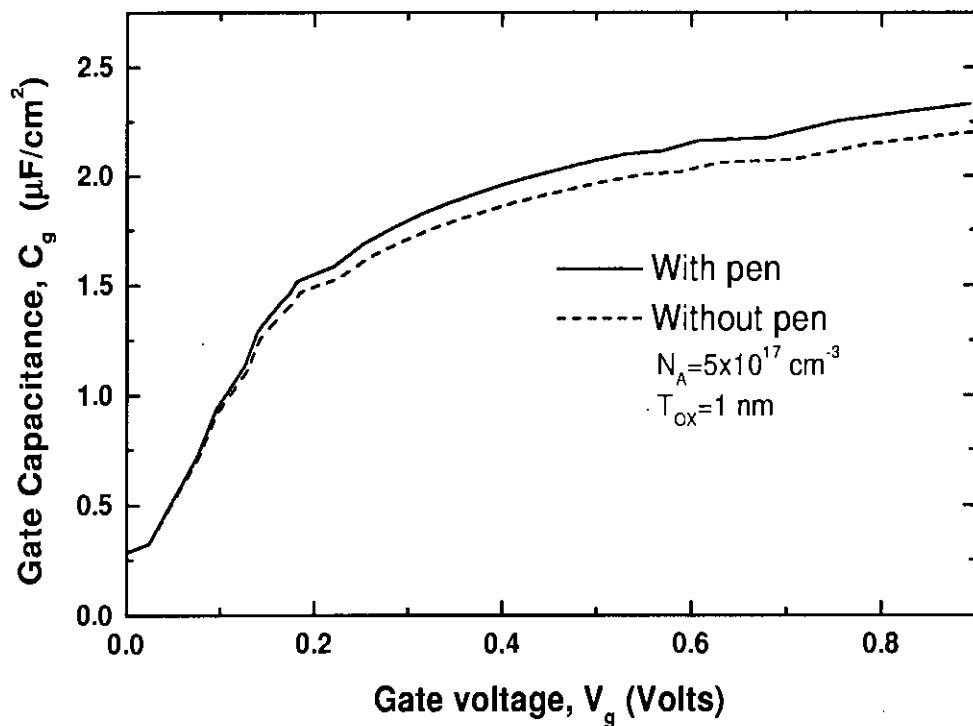


Fig. 3.8: Gate capacitance C_g vs V_g for (111) n-MOS. Calculations are for $N_A = 5 \times 10^{17} \text{ cm}^{-3}$ and $T_{\text{ox}} = 1 \text{ nm}$.

increases (so does N_{depl} and F_{ox}) and ϕ_I becomes a smaller fraction of the total gate voltage, thereby reducing the error in V_{DD} . It can, therefore, be concluded that when device dimensions are scaled down, the relative error in supply voltage due to neglect of wave function penetration is only weakly affected.

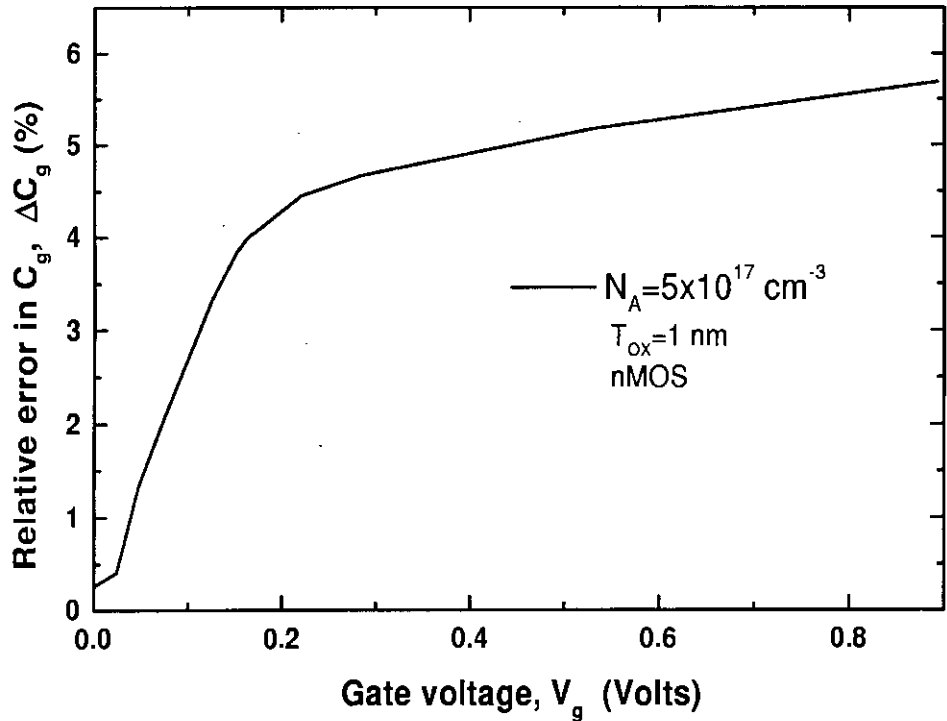


Fig. 3.9: Relative error in C_g , ΔC_g in (%), as a function of V_g for the device studied in Fig. 3.8.

3.3 n-MOS and p-MOS Devices for (100) silicon

Results for n-MOS and p-MOS devices on (100) silicon are presented in this section. Again, the results are calculated at room temperature. In our calculation for electrons, we have considered two valleys of the conduction band as mentioned earlier. For holes we have considered three types of bulk hole sub-bands, *i.e.*, light, heavy and split-off holes. The potential barrier height at silicon-oxide interface has been considered to be 4.78 eV for holes.

Figs. 3.11(a) and 3.11(b) are the plots of the average distance z_{avg} of the inversion carriers from the interface as a function of inversion carrier density, N_{inv} , for n-MOS and p-MOS devices, respectively. It can be seen in Fig. 3.11(a) that the average distance of the longitudinal valley electrons is much smaller than that

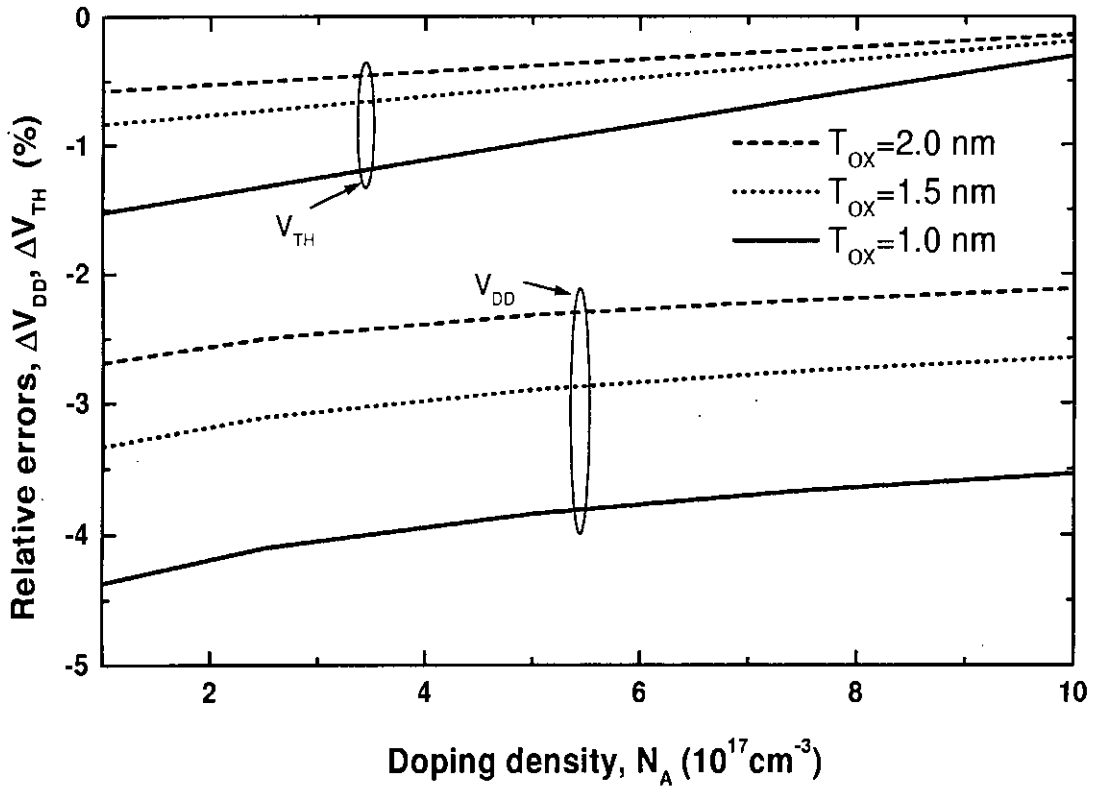


Fig. 3.10: Relative errors in threshold voltage, ΔV_{TH} , and in supply voltage ΔV_{DD} , as functions of doping density N_A . Calculations are for three oxide widths $T_{ox} = 1.0$ nm, 1.5 nm, 2.0 nm.

of the transverse valley electrons. It is due to the heavier effective mass of the longitudinal valley compared to the transverse valley. It can also be seen that the z_{avg} is closer to z_{avgl} for n-MOSFETs. This is because the carrier density associated with the longitudinal valley is greater. When we compare these results with those in Fig. 3.2 for (111) silicon devices, z_{avg} is found to be smaller for (100) devices. As already mentioned, heavier effective mass for longitudinal valley electrons in (100) silicon is responsible for this. Due to the same normal effective mass, m_z , of heavy holes and split-off holes, the average distances for both were found identical and results for split-off holes are not shown explicitly. z_{avg} for holes is found higher than that for electrons. This implies that holes, on the average, stay further away from the interface than electrons. Again, the reason behind this is the lower effective mass of holes. We, therefore, conclude

that lower effective mass of inversion carriers causes the average distance from the interface to increase. The results for holes are consistent with those obtained in Ref. [6].

Figs. 3.12(a) and 3.12(b) are the plots of the relative error in average distance, Δz_{avg} (in nm) of the inversion carriers from the interface as a function of inversion carrier density, N_{inv} , for n-MOS and p-MOS devices, respectively. It is observed that when penetration is not considered, z_{avg} is over-estimated by about 0.1 nm for electrons and 0.18 nm for holes. It indicates that the shift of average distance due to penetration is almost double for holes compared to electrons in (100) devices. As the barrier height at the silicon-oxide interface for holes is greater than that for electrons, it is commonly believed that penetration effects are more severe in n-MOS devices. However, our results indicate otherwise. Again, this can be explained in terms of the relative magnitude of effective masses of electrons and holes in different valleys. The penetration effect is also more severe for transverse valley electrons than for longitudinal valley electrons (similar observation also for holes). Thus, we can conclude that the penetration effect depends upon the effective mass of carriers and is more dominant for carriers with lower effective mass. An unusual feature observed in Fig. 3.12(a) is that for electrons, Δz_{avg} may decrease with increasing N_{inv} and at high inversion carrier density, Δz_{avg} for all electrons is actually smaller than the error for electrons either in the longitudinal or in the transverse valley. This odd result will be explained later in this section.

Figs. 3.13(a) and 3.13(b) are the plots of Δz_{avg} in percent of z_{avg} with penetration as a function of N_{inv} , for n-MOS and p-MOS devices, respectively. Since the value of the difference in z_{avg} remains almost constant for holes, its relative error increases with increasing N_{inv} due to decrease in z_{avg} . But due to the decrease in Δz_{avg} for electrons, its relative error decreases with increasing N_{inv} except at very high N_{inv} . We have also calculated z_{avg} for different gate oxide thickness. It is observed that oxide thickness has no significant effect on z_{avg} . Comparing Fig. 3.13 with Fig. 3.3, it is found that the relative error in average penetration is the maximum for electrons on (111) silicon devices. This observation is consistent with the remarks made in the discussion on Figs. 3.11 and 3.12 (see Tables 3.1

and 3.2).

Figs. 3.14, 3.15 and 3.16 are the plots of the relative concentrations of inversion carriers among different valleys as a function of inversion carrier density, N_{inv} , for three different doping densities, respectively. Results for both n-MOS and p-MOS devices are shown in each figure. From these figures, it can be seen that the relative concentrations of holes are almost independent of substrate doping and boundary conditions although these change slightly with N_{inv} . But for electrons, the relative concentrations are severely affected by the substrate doping, boundary conditions and N_{inv} . It can be seen that with increase in N_A , longitudinal valley becomes more dominant. The relative concentration for longitudinal valley increases with increasing N_{inv} , and that for the transverse valley decreases with increase in N_{inv} . Finally, if penetration is considered, the relative occupancy of longitudinal valley decreases with a corresponding increase in that of transverse valley. It has been numerically verified that the large difference between effective masses for electrons in longitudinal and transverse valleys and the corresponding small difference for heavy and light holes are responsible for the observed effects in these figures.

Figs. 3.17(a) and 3.17(b) are the plots of eigenenergies measured from Fermi energy, $(E_{ij} - E_F)$, as a function of inversion carrier density, N_{inv} , for n-MOS and p-MOS devices, respectively. From Fig. 3.17, it can be seen that for electrons $(E_{ij} - E_F)$ are sensitive to the penetration effects and the effects increase with increase in N_{inv} . In the longitudinal valley, $(E_{ij} - E_F)$ are under-estimated when penetration effects are neglected whereas in the transverse valley, neglect of penetration effects causes $(E_{ij} - E_F)$ to increase. But for holes, calculated $(E_{ij} - E_F)$ are almost independent of the boundary conditions. Since the probability of occupancy of any eigenstate depends on $(E_{ij} - E_F)$ according to Fermi-Dirac statistics, a change in this quantity with boundary condition results in the boundary condition dependence of relative concentration observed in Figs. 3.14, 3.15 and 3.16.

Figs. 3.18(a) and 3.18(b) are the plots of $(E_{ij} - E_F)$ as a function of substrate doping density, for n-MOS and p-MOS devices, respectively at an inversion car-

rier density of $N_{inv} = 10^{12} \text{ cm}^{-2}$. It can be seen that for electrons, penetration effects on $(E_{ij} - E_F)$ are sensitive to the change in doping density and are more dominant at higher substrate doping. But for holes, boundary conditions have no significant effect on $(E_{ij} - E_F)$, and this effect is very weakly dependent on doping density. Fig. 3.18 explains the doping density dependence of the relative concentration observed in Figs. 3.14, 3.15 and 3.16.

The unusual feature observed in Figs. 3.12 and 3.13 for electrons can now be explained. Δz_{avg} for a given N_{inv} is defined by the following relationship, $\Delta z_{avg} = z_{avg}^{wp} - z_{avg}^{np}$, where, 'wp' stands for with penetration and 'np' implies no penetration. Here for electrons,

$$z_{avg}^{wp} = \frac{1}{N_{inv}} [N_{invL}^{wp} z_{avgL}^{wp} + N_{invT}^{wp} z_{avgT}^{wp}], \quad (3.2)$$

and

$$z_{avg}^{np} = \frac{1}{N_{inv}} [N_{invL}^{np} z_{avgL}^{np} + N_{invT}^{np} z_{avgT}^{np}], \quad (3.3)$$

and similar expression apply for holes. Note that in Eqs. (3.2) and (3.3), $N_{invL}^{wp} + N_{invT}^{wp} = N_{invL}^{np} + N_{invT}^{np} = N_{inv}$.

For holes, penetration has no significant effect on relative concentrations of carriers. So, for holes, $N_{invL}^{wp} \cong N_{invL}^{np}$ and $N_{invH}^{wp} \cong N_{invH}^{np}$. Defining $\Delta z_{avgL} = z_{avgL}^{wp} - z_{avgL}^{np}$ and $\Delta z_{avgH} = z_{avgH}^{wp} - z_{avgH}^{np}$, we write for holes,

$$\Delta z_{avg} \cong \frac{1}{N_{inv}} [N_{invL}^{wp} \Delta z_{avgL} + N_{invH}^{wp} \Delta z_{avgH} + N_{invS}^{wp} \Delta z_{avgS}]. \quad (3.4)$$

Here $\Delta z_{avgS} = \Delta z_{avgH}$. So, Δz_{avg} will be a weighted average of Δz_{avgL} and Δz_{avgH} and Δz_{avg} will lie between the two.

But for electrons, significant changes in relative carrier concentrations in longitudinal and transverse valleys occur due to wave function penetration. In such case, Δz_{avg} will not be a simple weighted average of Δz_{avgL} and Δz_{avgT} . Dependence of Δz_{avg} on N_{inv} can be explained in terms of a sample calculation shown in Table 3.3.

From this calculation, it becomes evident that although the error for any given valley increases with increasing N_{inv} , due to different weighting factors associated

N_{inv} cm^{-2}	z_{avg} nm	N_{inv} 10^{10}cm^{-2}	z_{avg} nm	N_{inv} 10^{10}cm^{-2}	Δz_{avg} nm	Δz_{avg} nm	Δz_{avg} nm
10^{11}	1.671 (wp)	6.11 (wp)	2.421(wp)	3.89(wp)	-0.094	-0.072	-0.329
	1.743(np)	6.88(np)	2.75(np)	3.12(np)			
10^{13}	1.075(wp)	682(wp)	1.786(wp)	318(wp)	-0.074	-0.085	-0.434
	1.16(np)	798(np)	2.22(np)	202(np)			

Table 3.3: Sample calculation of Δz_{avg} for electrons.

with different boundary conditions, Δz_{avg} can decrease with increase in N_{inv} and can even become less than either Δz_{avg} or Δz_{avg} .

Figs. 3.19(a) and 3.19(b) show C_{inv} as a function of N_{inv} calculated using both the boundary conditions for n-MOS and p-MOS devices, respectively. It can be seen that the inversion layer capacitance calculated for both n-MOS and p-MOS devices without considering penetration are identical to those obtained in Ref. [12] from self-consistent calculations for (100) silicon devices. This indicates the accuracy of our numerical calculation. At strong inversion, C_{inv} for electrons is higher than that for holes. We also find that penetration effects are more in p-MOS structures. Comparison of Fig. 3.19 with Fig.3.6 reveals that penetration effects are the most visible for (111) nMOSFETs.

Figs. 3.20(a) and 3.20(b) are the plot of ΔC_{inv} , the relative error in C_{inv} as a function of N_{inv} , for n-MOS and p-MOS devices, respectively. Again, we find that oxide thickness has no effect on calculation of C_{inv} . A significant finding in Fig. 3.20 is that the effect of substrate doping on relative error in C_{inv} is opposite for n-MOS and p-MOS devices. The relative error increases for holes, whereas decreases for electrons with increasing doping density. It is because in (100) structures for a given N_{inv} , Δz_{avg} decreases for electrons with increasing doping density, while Δz_{avg} increases for holes with increasing doping density. Also the percentage error is greater for holes. A comparison of Fig. 3.20 with Fig. 3.7 shows that the effects of doping density on (111) n-MOS are similar to those for (100) p-MOS.

Figs. 3.21(a) and 3.21(b) are the plot of C_g as a function of V_g , for n-MOS and p-MOS devices, respectively. Results show that C_g is under-estimated when

penetration effects are not considered and the error is more at higher gate voltages. Moreover, wave function penetration has more influence on C_g for p-MOS rather than for n-MOS. This apparently small error in C_g due to penetration will have non-trivial effects on device parameter extraction from C-V measurements.

Figs. 3.22(a) and 3.22(b) are the plot of ΔC_g (%) as a function of V_g , for n-MOS and p-MOS devices, respectively. The results show some interesting trends. The error is negligible in the sub-threshold region, increasing sharply around threshold and becomes almost linear in inversion region. Since increasing doping density increases the threshold voltage of a MOSFET, ΔC_g curves are shifted to the right with increase in doping density. For n-MOS structures, there is a decrease in the error with an increase in N_A in the strong inversion region. On the other hand, for p-MOS devices, the error is almost independent of doping density in strong inversion. These results are explained in the following way with the help of Fig. 3.20. In MOSFETs with a given V_g , N_{inv} is higher for a device with lower substrate doping density. Thus for a fixed V_g , a point in Fig. 3.22 for a curve with higher doping density corresponds to a lower N_{inv} . Now in Fig. 3.20, we find for electrons that as doping density increases, ΔC_{inv} for the same N_{inv} decreases. Consequently, the reduction in ΔC_{inv} is even greater when N_{inv} is also reduced (to keep V_g fixed). Since, C_g is the series combination of C_{ox} and C_{inv} , a reduction in error in C_{inv} , in turn, reduces the error in C_g with an increase in N_A . Therefore, in strong inversion ΔC_g is reduced as N_A increases. Fig. 3.20(b) for holes show that the dependence of ΔC_{inv} on N_D is opposite to that for electrons. When doping density increases for a fixed N_{inv} , the error increases. A decrease in N_{inv} (to keep V_g fixed) then reduces the error. Due to these competing effects in ΔC_{inv} , the resulting error in C_g essentially becomes independent of substrate doping density for p-MOSFETs in strong inversion.

Figs. 3.23(a) and 3.23(b) are the plots of ΔC_g (%) as a function of V_g , for n-MOS and p-MOS devices, respectively. The plots are for a certain substrate doping density but different oxide thickness. It can be seen that with decrease in oxide thickness, the relative error in C_g increases for both n-MOS and p-MOS devices but the error is much higher for the later devices. This results can be

explained with the help of electrical oxide thickness, T_{ele} . Gate capacitance is inversely proportional to T_{ele} where electrical oxide thickness, (T_{ele}) is given by, $T_{ele} = T_{ox} + (\epsilon_{ox}/\epsilon_{si})z_{avg}$ [8]. With scaling down of MOSFET device dimensions, T_{ox} decreases and substrate doping density increases. But as the relative error in z_{avg} is independent of oxide thickness, the same percentage error in estimating z_{avg} will have a much greater effect on T_{ele} or $C - g$ with decrease in oxide thickness.

From the results presented so far, we can compare the effects of wave function penetration on surface orientation of the n-MOS devices. Comparing the results for (111) and (100) electrons, we conclude that penetration effects are more severe for the (111) orientation. (111) silicon has only one bulk subband in the conduction band with six valleys of degeneracy, having an effective mass ($m_z = 0.258$) which is much lower than that for an electron in the longitudinal valley ($m_l = 0.916$) in (100) silicon. Due to the lower effective mass of electrons in (111) silicon, the average distance of carrier from the interface is high and the effect of penetration is more. Another, important finding is that the dependence of the relative error in C_{inv} on doping density is opposite for devices on (111) and on (100) silicon.

We can now summarize the comparison of penetration effects on n-MOSFET and p-MOSFET on (100) silicon. As the barrier height for holes is greater than that for electrons, penetration effects were expected to be more severe for n-MOS devices. But, from Figs. 3.12 and 3.13, we found that the penetration effect actually is more severe for p-MOS devices. It is due to the lower effective mass of the heavy holes compared to that of electrons in the longitudinal valley. The effect of doping density on gate capacitance of both p-MOS and n-MOS structures are presented in Figs. 3.20 and 3.22. It can be seen that with an increase in substrate doping density, ΔC_g vs V_g curve is shifted to the right due to an increase in the threshold voltage. For, n-MOS devices, ΔC_g decreases in strong inversion with increase in doping density, but for p-MOS devices, ΔC_g in strong inversion is more or less independent of doping density.

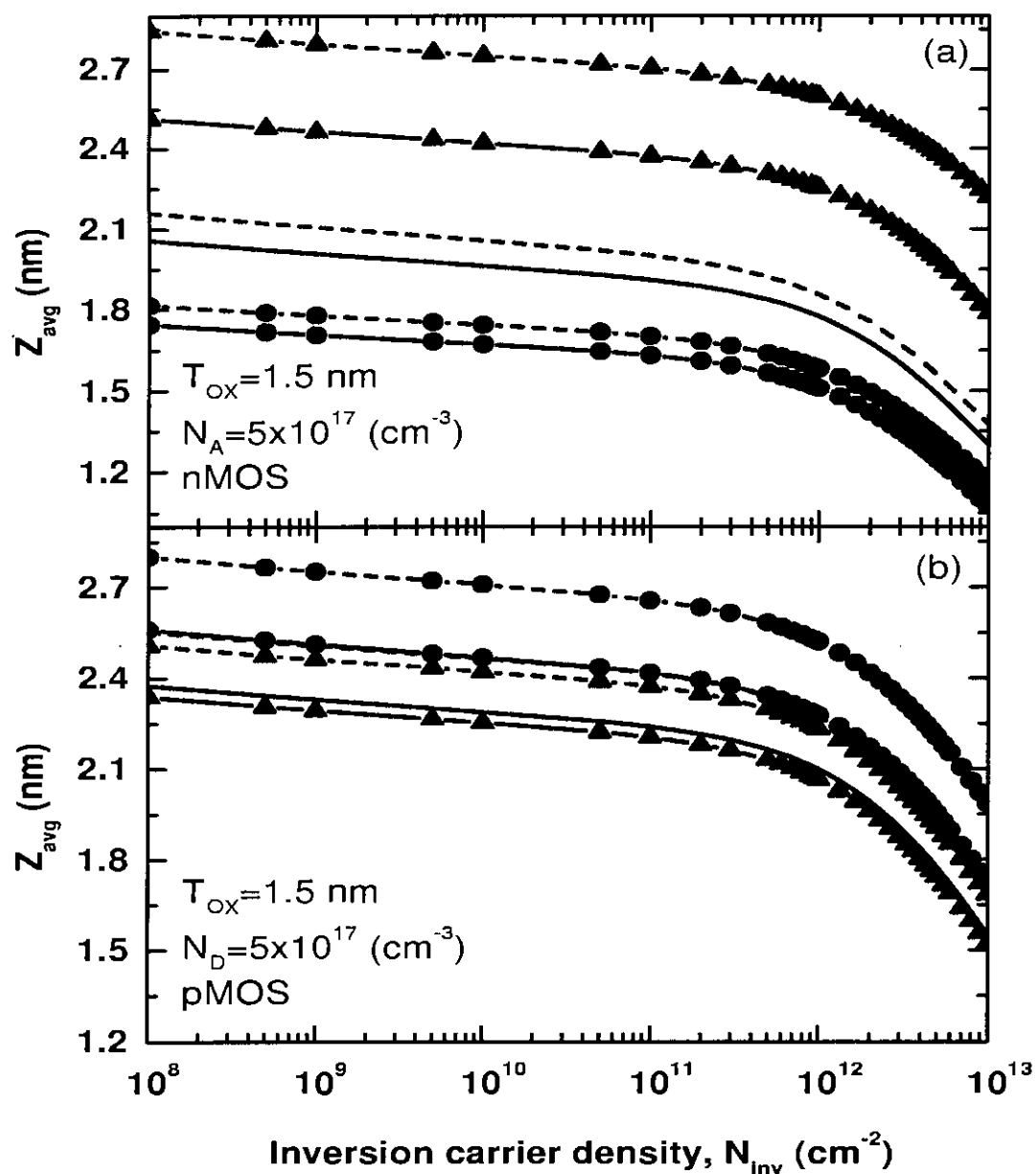


Fig. 3.11: Average distance of the inversion carriers from the interface, z_{avg} vs N_{inv} , for n-MOS and p-MOS, respectively. Solid lines indicate quantities with penetration and dashed lines indicate quantities without penetration. (a) for n-MOS, lines without any symbol indicate z_{avg} , lines with circle indicate z_{avgL} and lines with up-triangle indicate z_{avgH} . (b) for p-MOS, lines without any symbol indicate z_{avg} , lines with circle indicate z_{avgL} and lines with up-triangle indicate z_{avgH} .

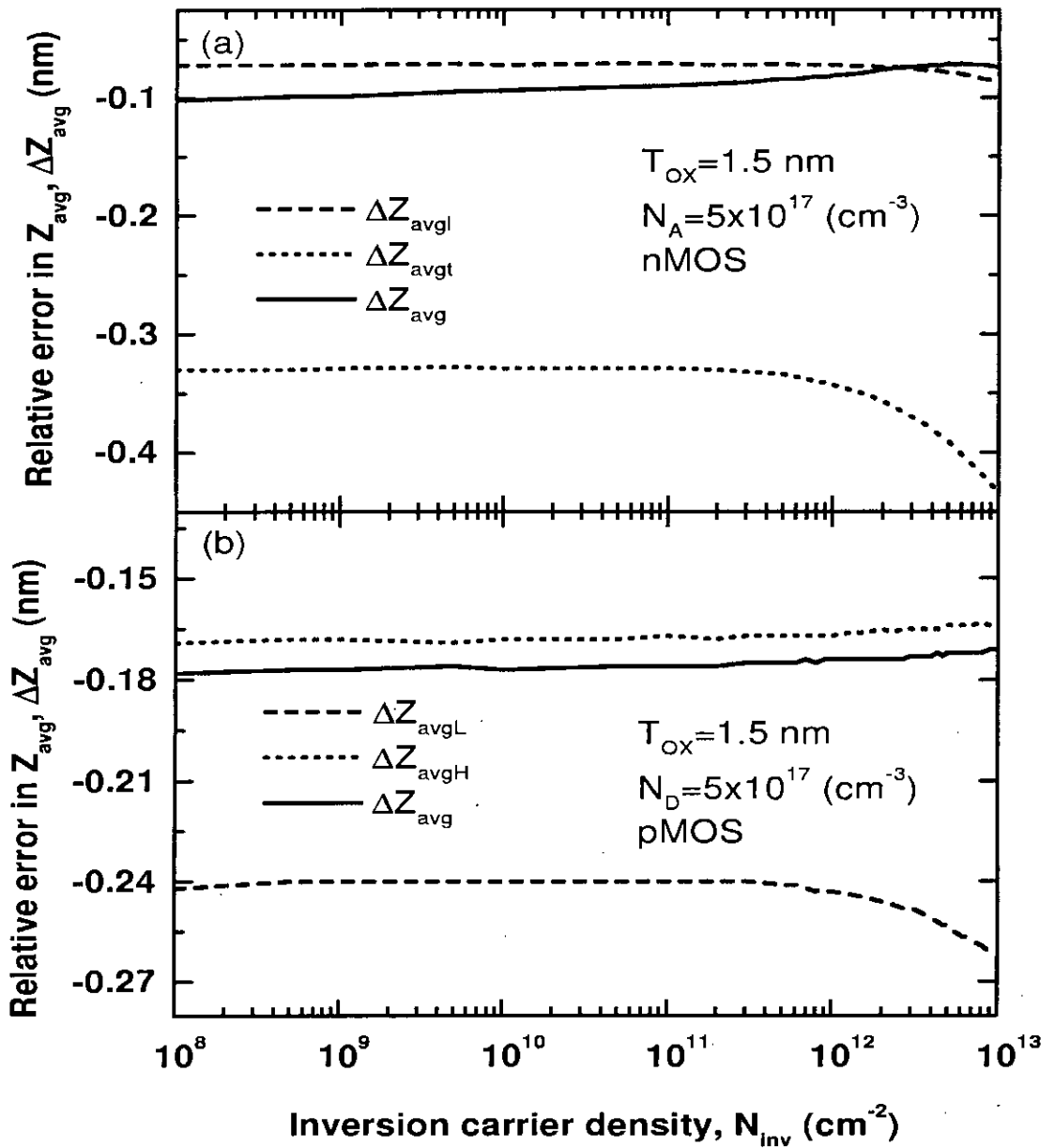


Fig. 3.12: Relative error in z_{avg} , Δz_{avg} in nm, as a function of N_{inv} for both (a) n-MOS and (b) p-MOS, respectively. Calculations are for oxide width, $T_{ox} = 1.5 \text{ nm}$ and doping density, $N_A = 5 \times 10^{17} \text{ cm}^{-3}$.

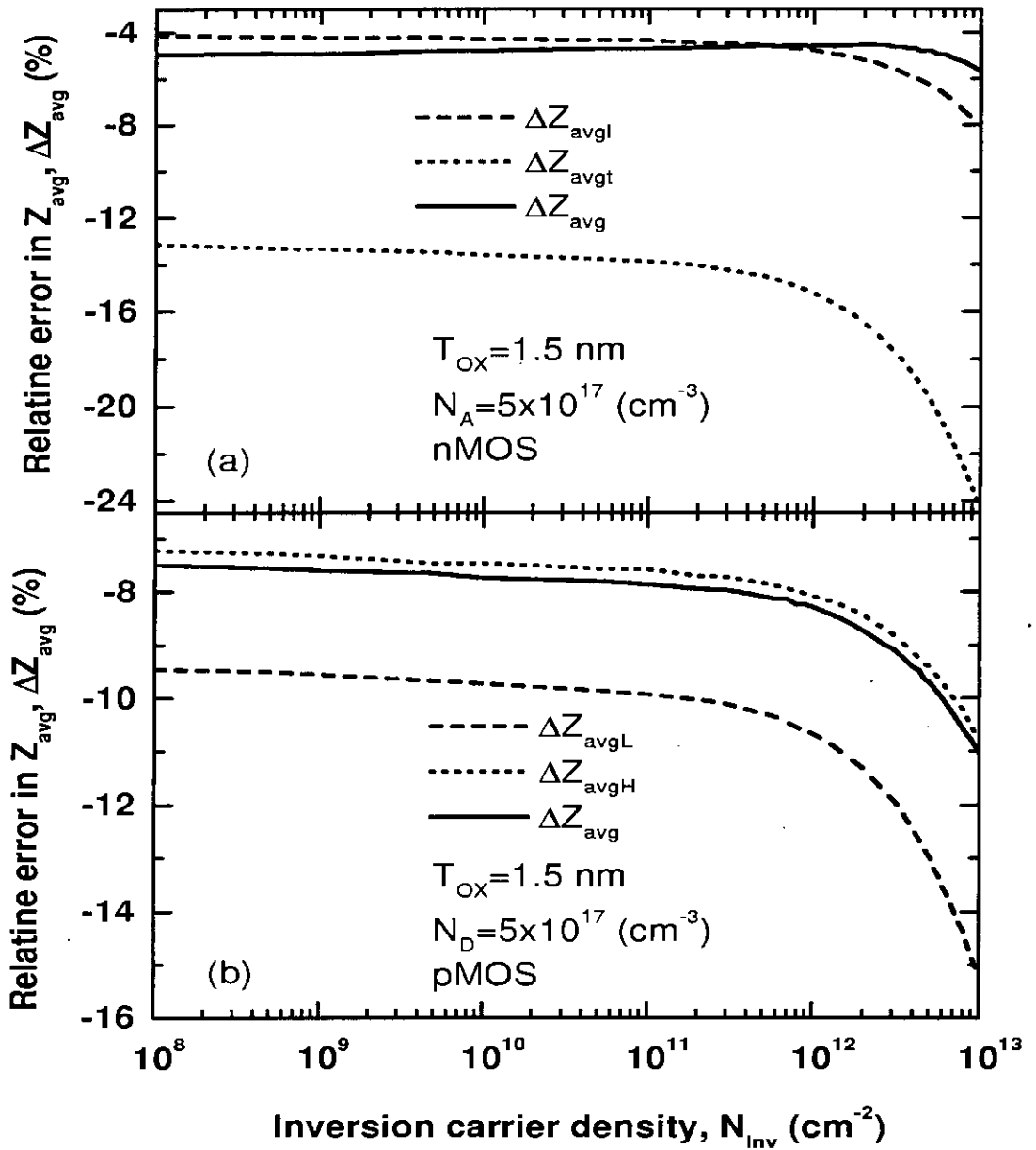


Fig. 3.13: Relative error in z_{avg} , Δz_{avg} in (%), as a function of N_{inv} for both (a) n-MOS and (b) p-MOS devices, respectively. Calculations are for oxide width, $T_{ox} = 1.5$ nm and doping density, $N_A = 5 \times 10^{17}$ cm^{-3} .

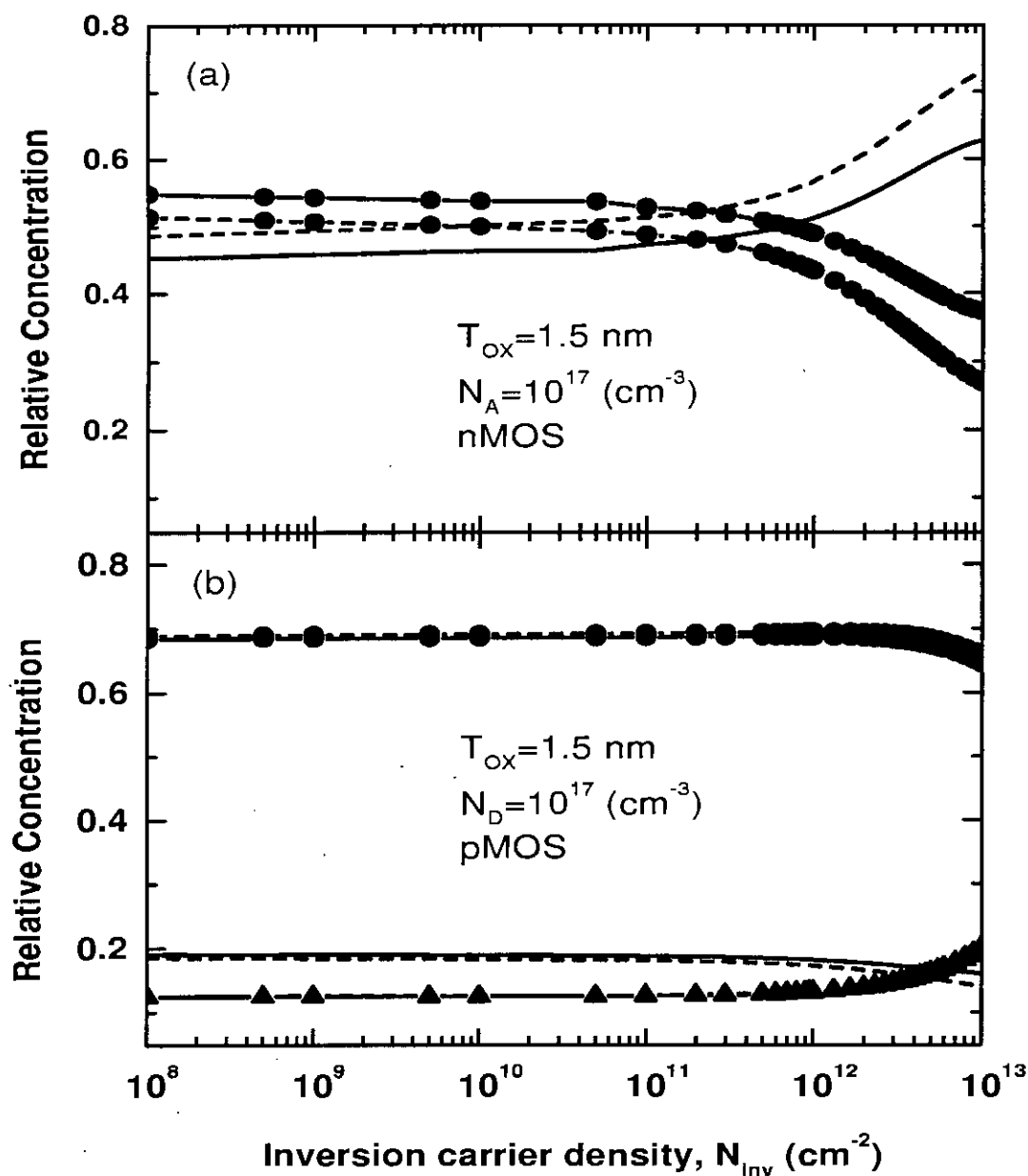


Fig. 3.14: Relative concentrations of the inversion carriers in different valleys as a function of N_{inv} . Calculations are for oxide width, $T_{ox} = 1.5$ nm and doping density, $N_A = 10^{17}$ cm^{-3} . Solid lines indicate quantities with penetration and dashed lines indicate quantities without penetration. (a) For n-MOS, lines without any symbol indicate relative concentration of longitudinal valley and lines with circle indicate relative concentration of transverse valley. (b) For p-MOS, lines without any symbol indicate relative concentration of light holes, lines with circle indicate relative concentration of heavy holes and lines with up-triangle indicate relative concentration of split-off holes.

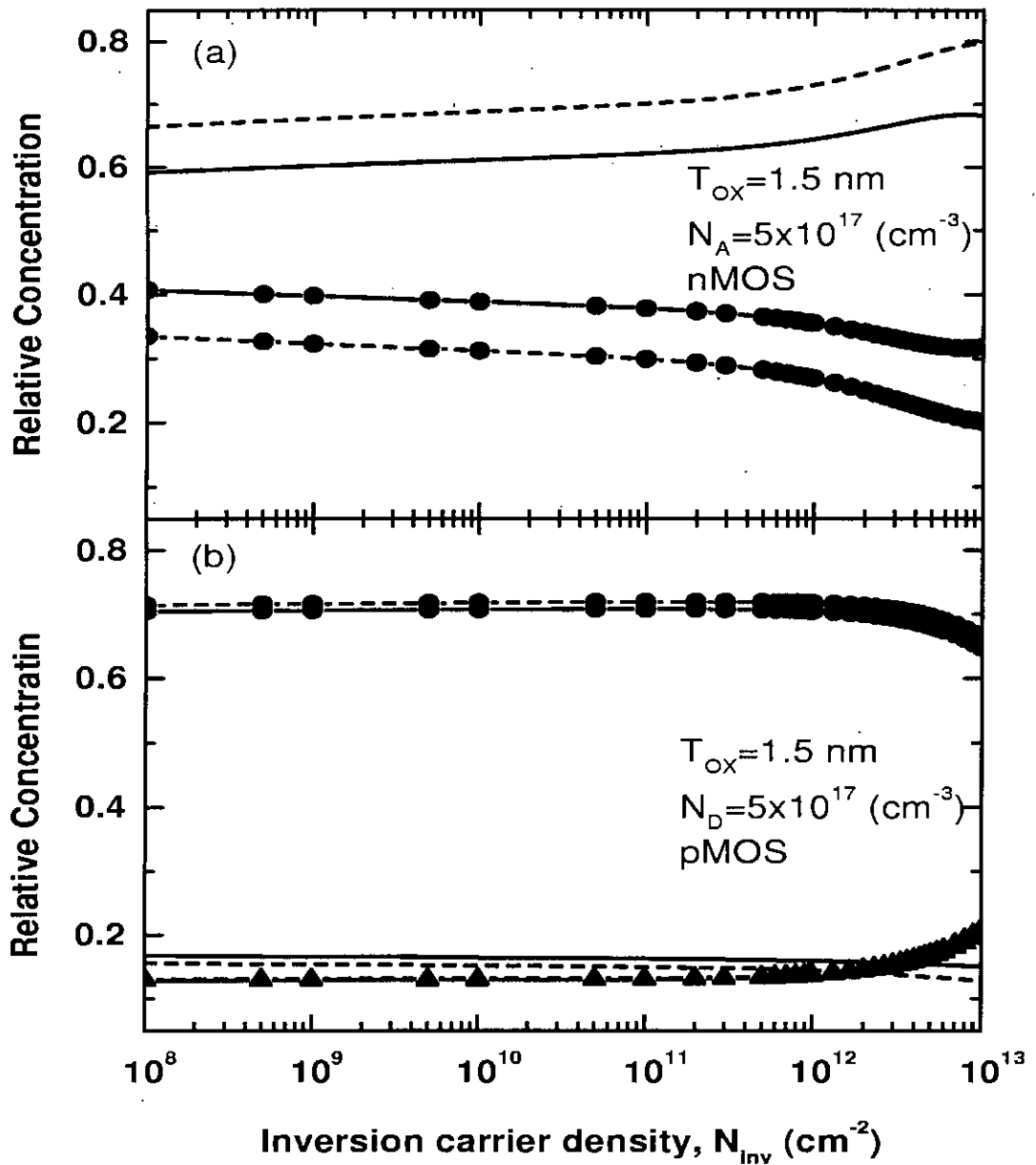


Fig. 3.15: Relative concentrations of the inversion carriers in different valleys as a function of N_{inv} . Calculations are for oxide width, $T_{ox} = 1.5 \text{ nm}$ and doping density, $N_A = 5 \times 10^{17} \text{ cm}^{-3}$. Solid lines indicate quantities with penetration and dashed lines indicate quantities without penetration. (a) For n-MOS, lines without any symbol indicate relative concentration of longitudinal valley and lines with circle indicate relative concentration of transverse valley. (b) For p-MOS, lines without any symbol indicate relative concentration of light holes, lines with circle indicate relative concentration of heavy holes and lines with up-triangle indicate relative concentration of split-off holes.

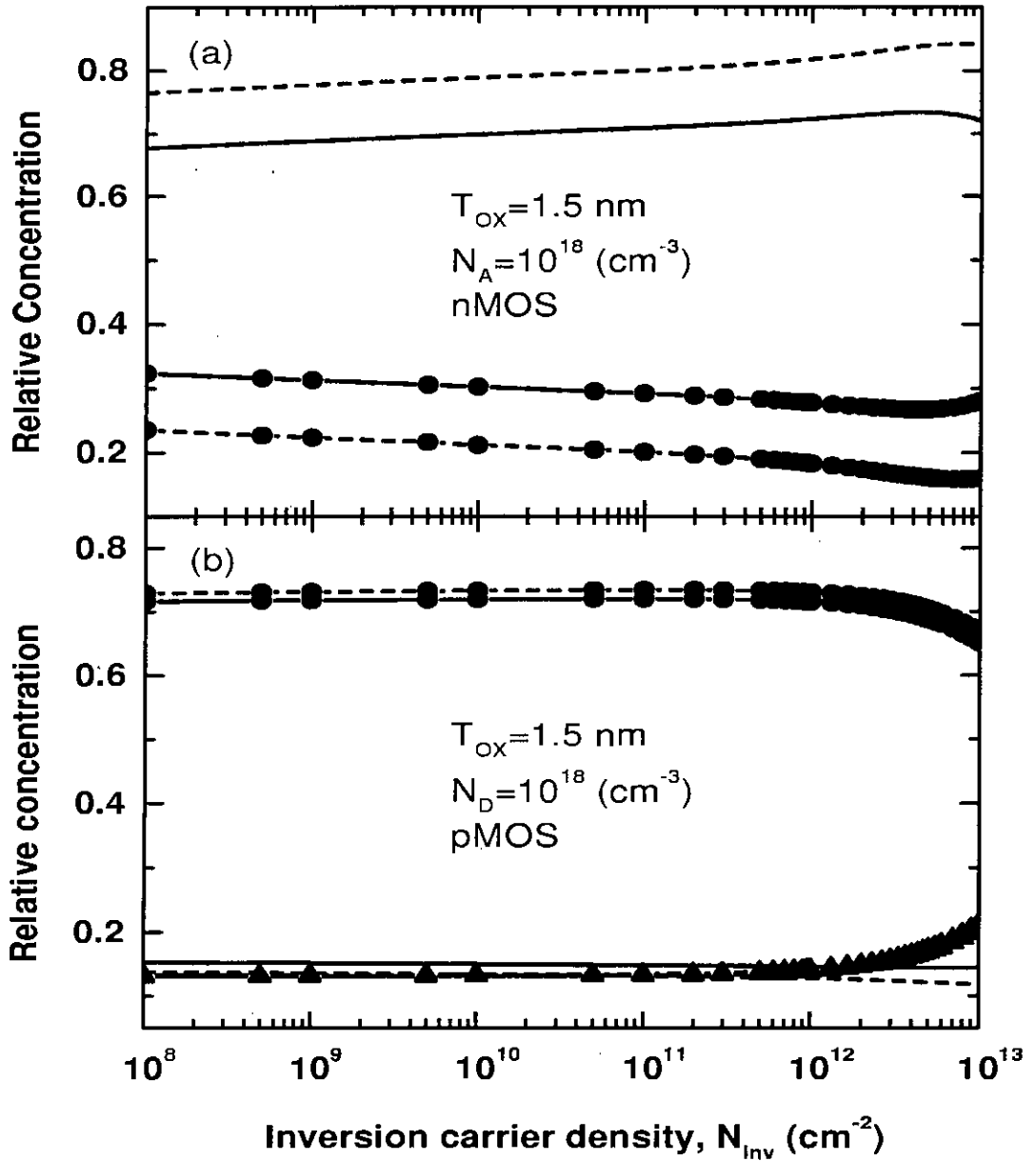


Fig. 3.16: Relative concentrations of the inversion carriers in different valleys as a function of N_{inv} . Calculations are for oxide width, $T_{ox} = 1.5 \text{ nm}$ and doping density, $N_A = 10^{18} \text{ cm}^{-3}$. Solid lines indicate quantities with penetration and dashed lines indicate quantities without penetration. (a) For n-MOS, lines without any symbol indicate relative concentration of longitudinal valley and lines with circle indicate relative concentration of transverse valley. (b) For p-MOS, lines without any symbol indicate relative concentration of light holes, lines with circle indicate relative concentration of heavy holes and lines with up-triangle indicate relative concentration of split-off holes.

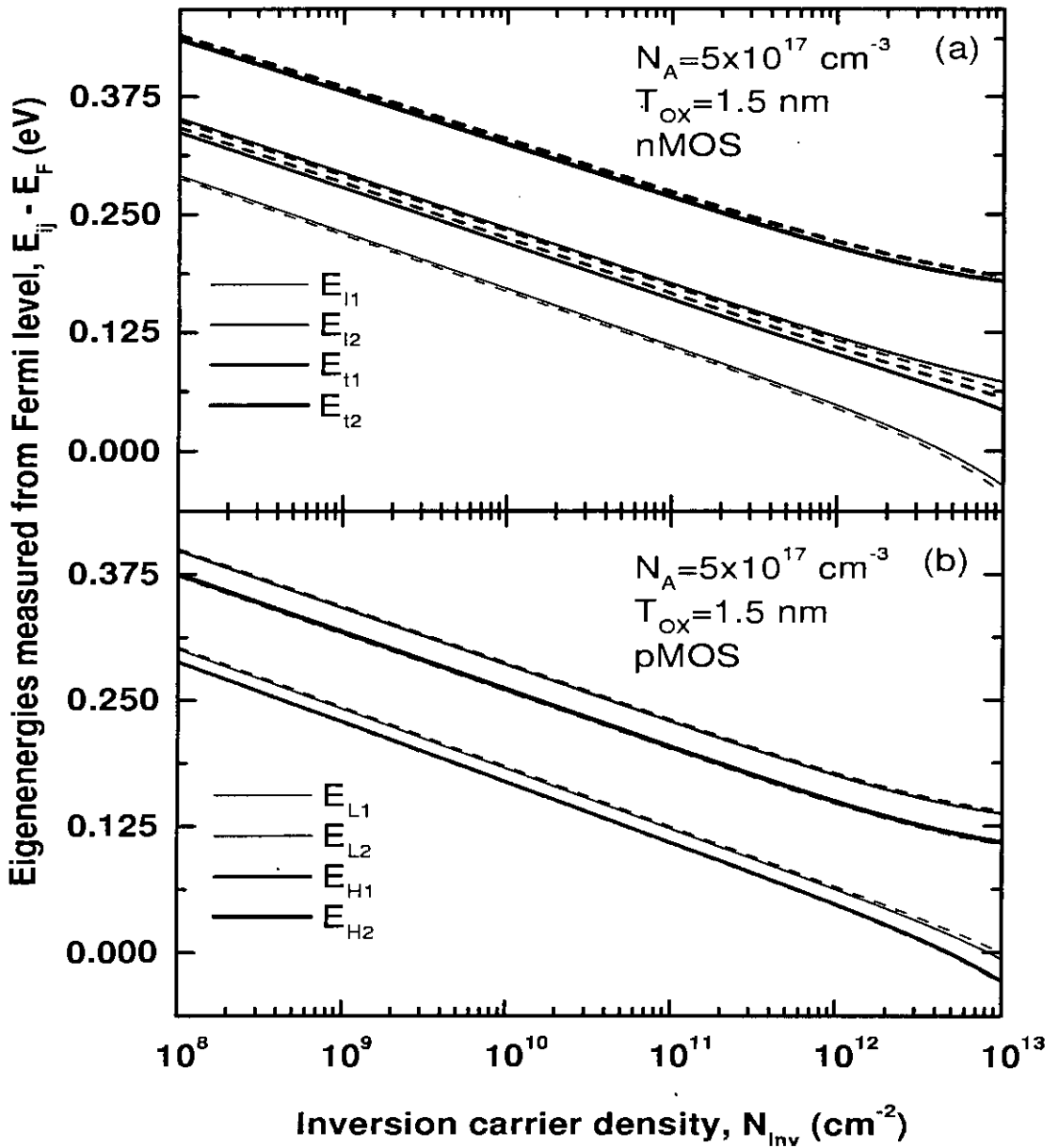


Fig. 3.17: Different eigenenergies measured from Fermi energy as a function of N_{inv} . Calculations are for oxide width, $T_{ox} = 1.5 \text{ nm}$ and doping density, $N_A = 5 \times 10^{18} \text{ cm}^{-3}$. Solid lines indicate quantities with penetration and dashed lines indicate quantities without penetration. (a) For n-MOS and (b) For p-MOS.

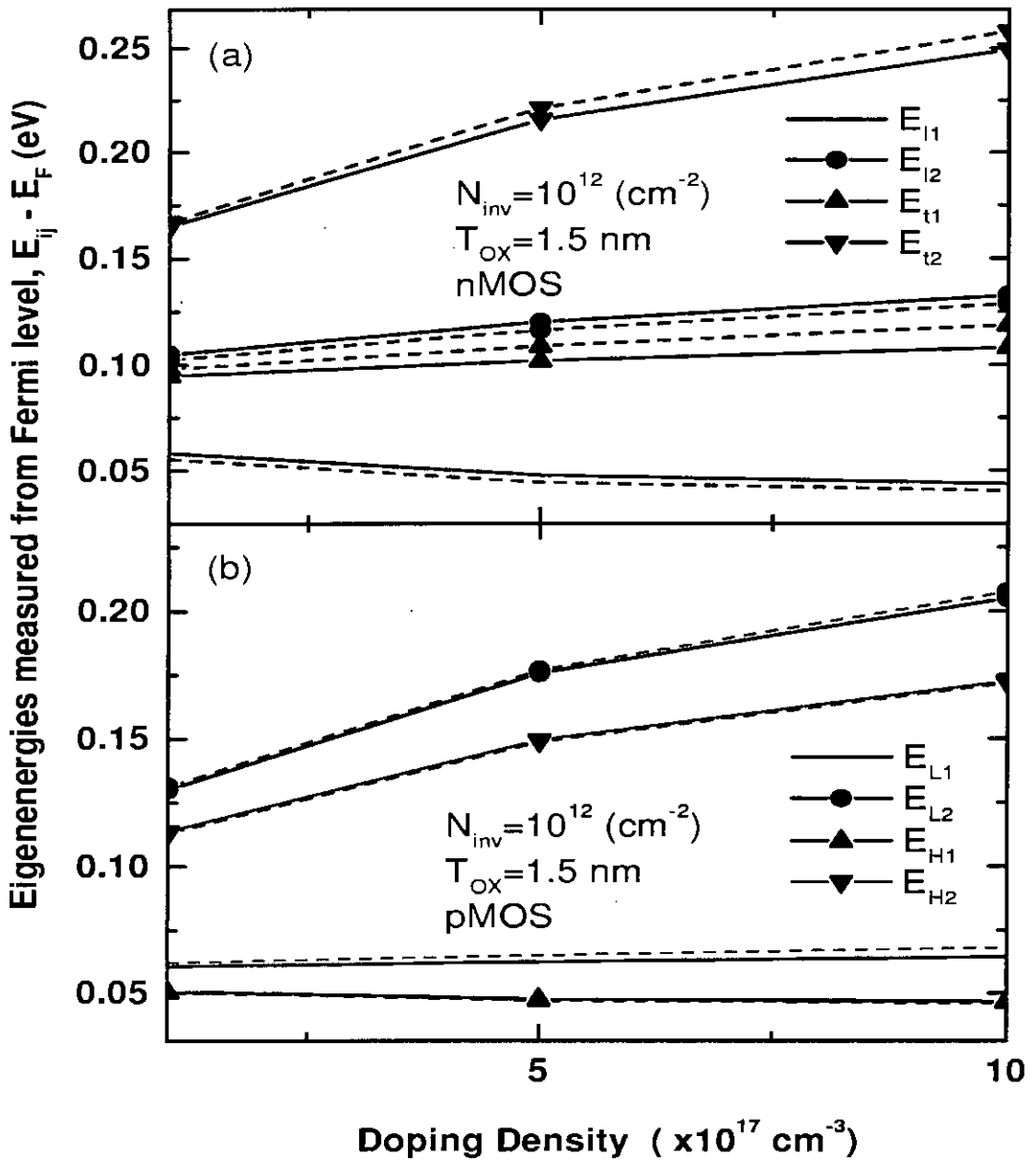


Fig. 3.18: Different eigenenergies measured from Fermi energy as a function of doping density, for (a) n-MOS and (b) p-MOS devices, respectively. Calculations are for oxide width, $T_{ox} = 1.5 \text{ nm}$ and inversion carrier density, $N_{inv} = 10^{12} \text{ cm}^{-2}$. Solid lines indicate quantities with penetration and dashed lines indicate quantities without penetration.

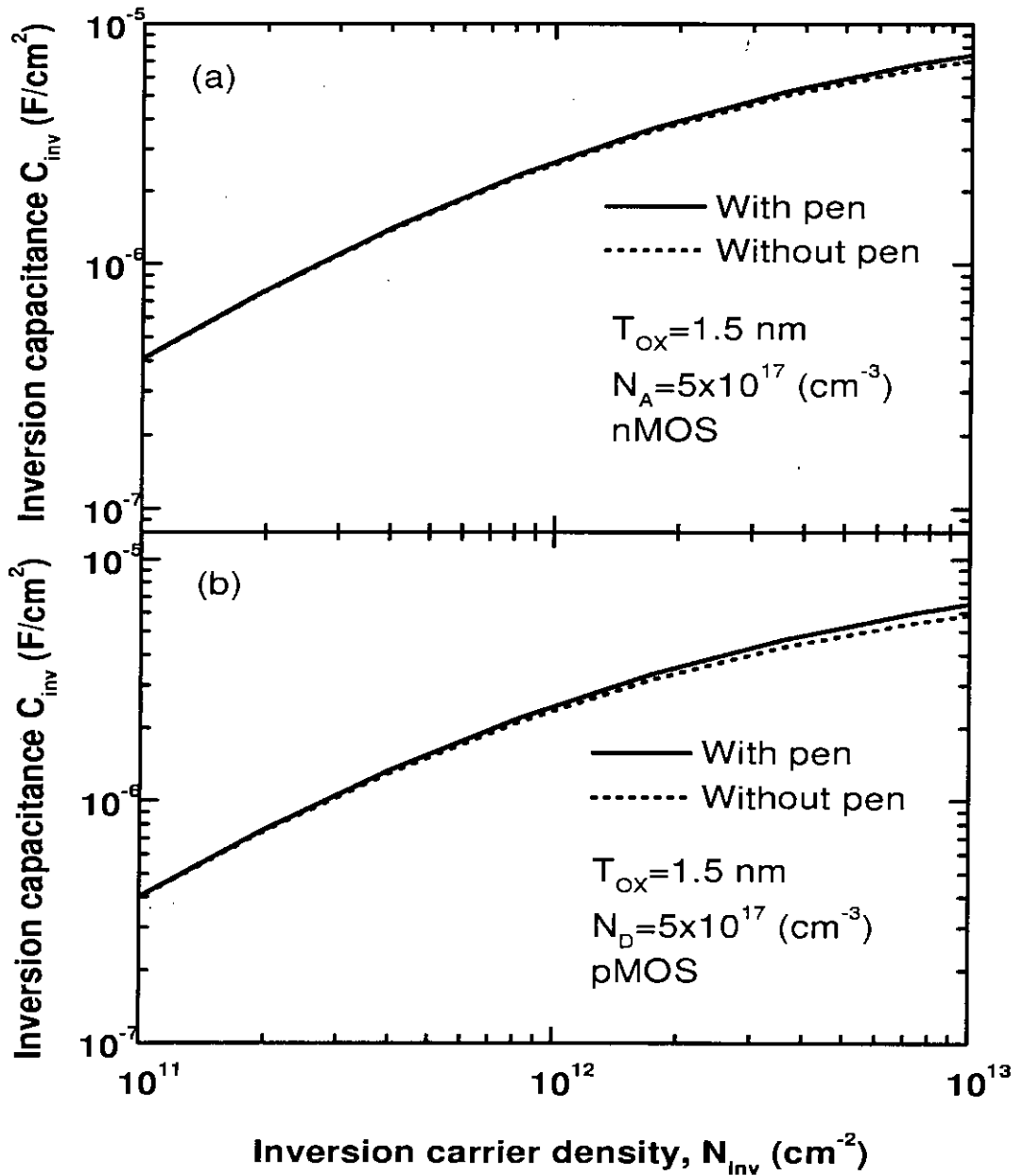


Fig. 3.19: Inversion capacitance C_{inv} vs N_{inv} for (a) n-MOS and (b) p-MOS devices, respectively. Calculations are for, $N_A = 5 \times 10^{17}$ cm^{-3} and $T_{ox} = 1.5$ nm.

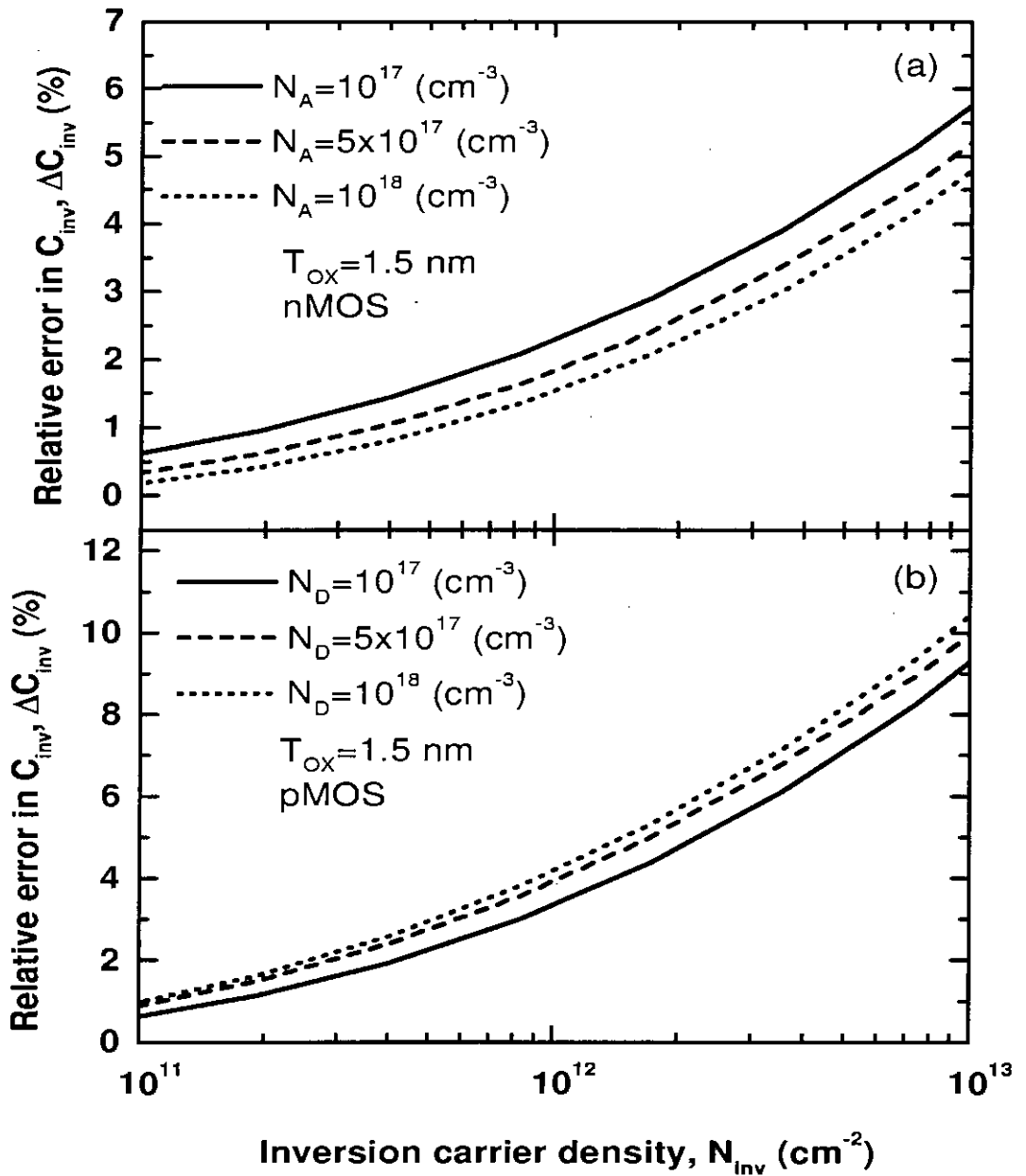


Fig. 3.20: Relative error in C_{inv} , ΔC_{inv} , as a function of N_{inv} for (a) n-MOS and (b) p-MOS devices, respectively. Calculations are for $T_{ox} = 1.5$ nm and $N_A = 10^{17}$ cm^{-3} , 5×10^{17} cm^{-3} and 10^{18} cm^{-3} .

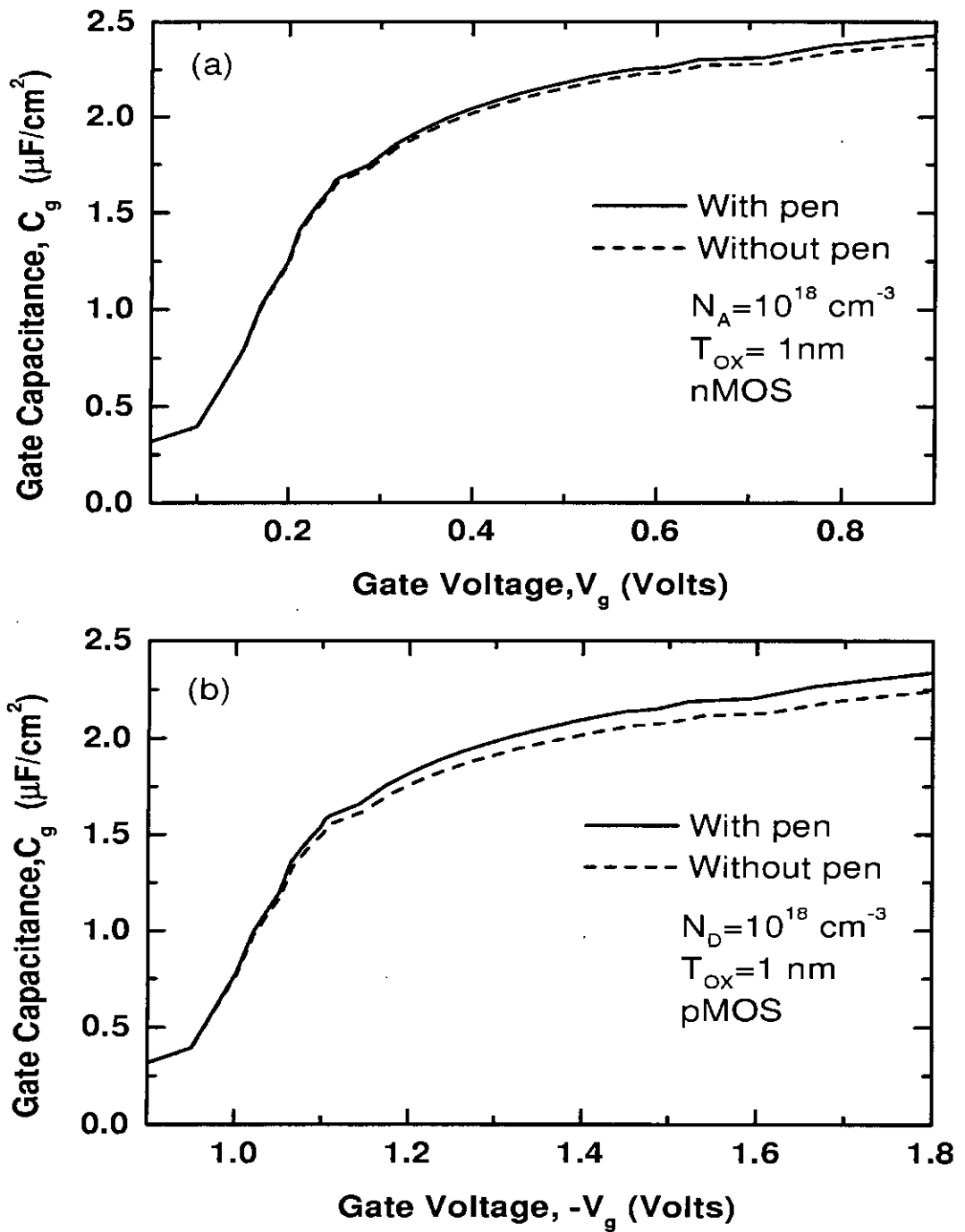


Fig. 3.21: Gate capacitance C_g vs V_g for (a) n-MOS and (b) p-MOS devices, respectively. Calculation are for, $N_A = 10^{18} \text{ cm}^{-3}$ and $T_{\text{ox}} = 1 \text{ nm}$.

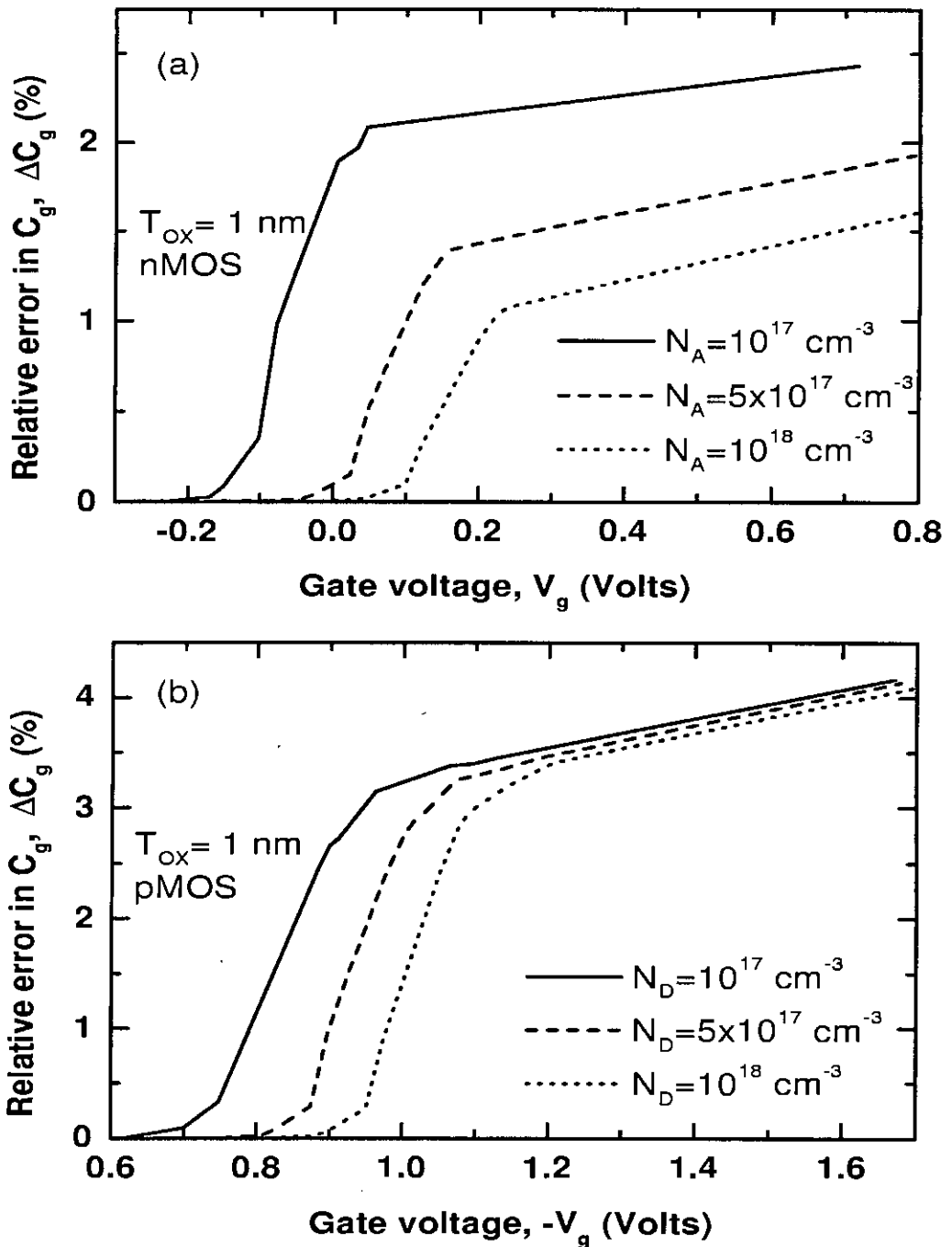


Fig. 3.22: Relative error in C_g , ΔC_g in (%), as a function of V_g for (a) n-MOS and (b) p-MOS respectively. Calculations are for $T_{ox} = 1 \text{ nm}$ and $N_A = 10^{17} \text{ cm}^{-3}$, $5 \times 10^{17} \text{ cm}^{-3}$ and 10^{18} cm^{-3} .

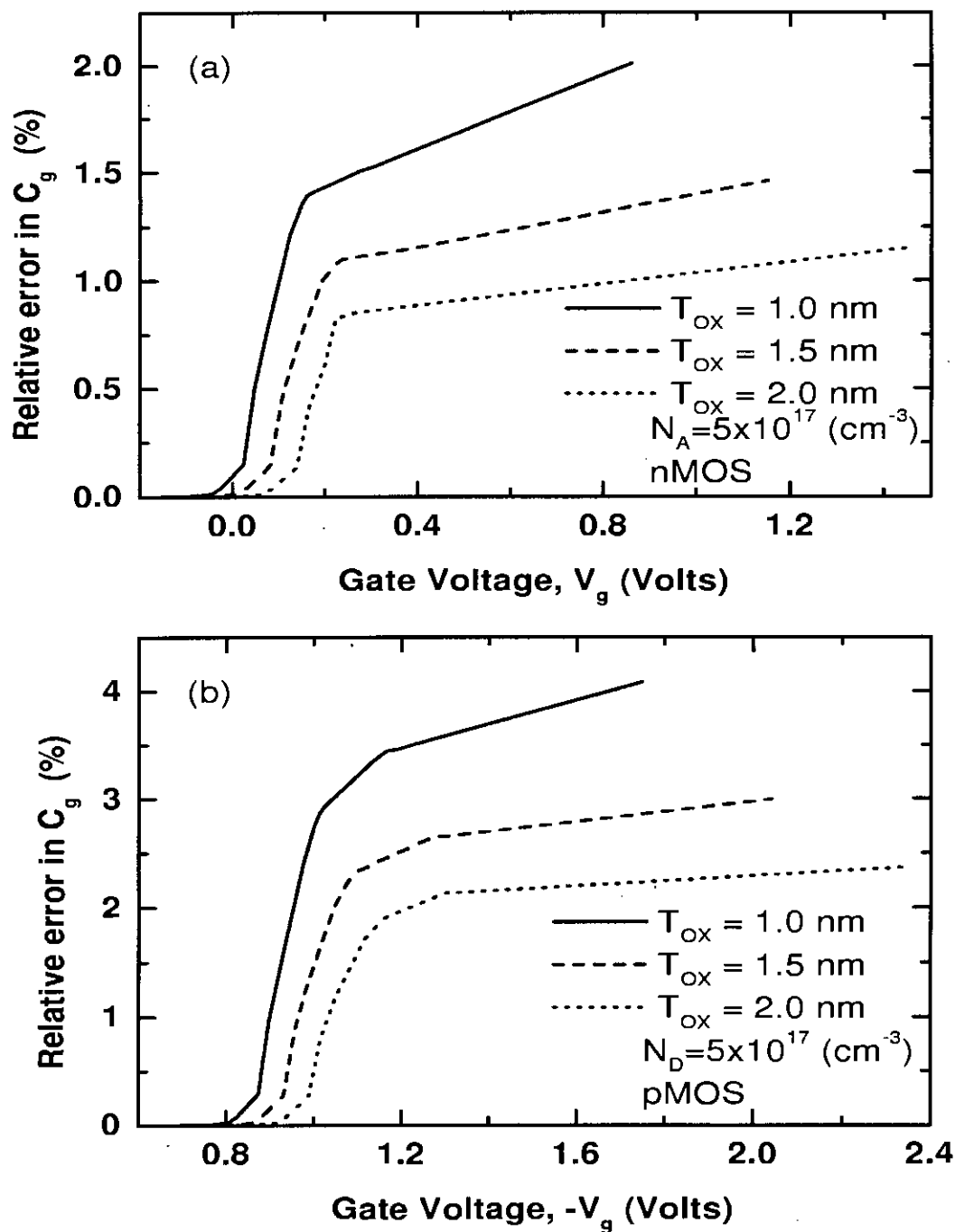


Fig. 3.23: Relative error in C_g , ΔC_g in (%), as a function of V_g for (a) n-MOS and (b) p-MOS respectively. Calculation are for $T_{ox} = 1$ nm, 1.5 nm, 2 nm, and $N_A = 5 \times 10^{17} \text{ cm}^{-3}$.

Chapter 4

Conclusion

An improved and numerically efficient self-consistent model has been proposed for MOSFET simulation which incorporates the wave function penetration into the gate oxide region. This new model is used to study the effects of wave function penetration on n-MOS and p-MOS devices by comparing the numerical results with those of the existing self-consistent model.

4.1 Summary

Effects of wave function penetration into gate oxide on properties of n-MOS and p-MOS devices in deep submicron regime are studied. Penetration effects are included within the self-consistent loop by solving both Schrödinger's and Poisson's equations taking into account wave function penetration. A new technique based on Green's function formalism has been used for the solution of Schrödinger's equation. Under this technique the solution of Schrödinger's equation, *i.e.*, eigenenergies and wavefunctions are found using the logarithmic derivative of Green's function which is calculated using a method analogous to the impedance transformation technique of microwave transmission lines with open boundary conditions. So, no matrix manipulation is required for the solution of Schrödinger's equation and the whole technique is numerically efficient. Poisson's equation is solved for the combined oxide and semiconductor regions by applying an appropriate boundary condition at the gate metal-oxide interface.

Numerical results for n-MOS devices on (111) silicon show that when the effects of wave function penetration are not considered within the self-consistent

loop, the errors made in estimating the electrostatic potential and the values of eigenenergies are non-trivial. Penetration effects on properties of inversion carriers become more important as device dimensions are scaled down. In particular, the effects are more pronounced when the devices are operating in strong inversion. It is observed that penetration effects on threshold voltages are insignificant. However, the effects on supply voltage, defined as the gate voltage required to induce certain inversion carrier density, can be as high as a few percents. Increase in doping density and reduction in oxide thickness have two opposing effects on the error made in estimating supply voltage when penetration effects are not considered. Consequently, effects of wave function penetration on supply voltage are weakly sensitive to device scaling. Comparison of numerical results for n-MOS and p-MOS structures on (100) silicon shows that contrary to the common belief, penetration effects are more pronounced in p-MOSFETs. This is found to be due to lower effective mass of heavy holes compared to that for electrons in the longitudinal valley. Variation of doping density has opposite effects on the relative error in inversion capacitance for n-MOS and p-MOS devices. These opposite trends manifest themselves in the relative error in gate capacitance in an interesting way. Error in gate capacitance is insignificant in the sub-threshold region and increases sharply around threshold. For n-MOS devices in strong inversion, relative error in gate capacitance decreases with increasing doping density, while that for a p-MOSFET is insensitive to doping density. Large difference in effective masses of electrons in longitudinal valley and in transverse valley compared to that of heavy and light holes are found to be responsible for this effect. Although the error in gate capacitance is only a few percent, this will have non-trivial effects on MOSFET parameter extraction from C-V measurements. Comparison of numerical results for n-MOS structures on (111) and (100) silicon shows that penetration effects are more pronounced in n-MOSFETs on (111) silicon. This is found to be due to the lower effective mass of electron in (111) silicon. The dependence of the relative error in C_{inv} on doping density is opposite for devices on (111) and on (100) silicon. Large difference in effective masses of (100) electrons in longitudinal valley and in transverse valley is found to be responsible for this effect.

4.2 Suggestions for Future Work

Self-consistent solution is an important tool for simulation of many devices where the QM effects become significant. Our self-consistent model may be used for simulating many systems, such as high electron mobility transistor (HEMT), resonant tunneling diodes and quantum well lasers, where self-consistent calculation with open boundary conditions is necessary. A few suggestions for future work is given below.

We have applied our model to calculate device properties in depletion and inversion regions. Certain modifications of the model is necessary to use it for simulating the accumulation region. Calculation of gate-capacitance accurately in accumulation is important from a parameter extraction point of view.

We have performed 1-D self-consistent solution of a MOS capacitor. But when voltage is applied between the drain and the source, quantum effects of 2-D nature arise in the channel and source/drain region of scaled ULSI MOS device, which may not be properly accounted for by 1-D or quasi 2-D approaches. So, to take into account the effects of the 2-D quantization, the existing 1-D self-consistent model should be modified.

The direct tunneling gate current of a deep submicron MOSFET flows due to QM tunneling of inversion layer carriers from semiconductor to the gate electrode. Our model may be applied for accurate determination of direct tunneling current.

As the gate length of CMOS devices are continued to be scaled down to sub-100 nm regime, scaling rules dictate that the gate oxide thickness be scaled down to well below 2 nm. As the thickness is decreased below 2 nm, the direct tunneling gate current increases rapidly. In order to decrease this leakage current, high-K materials should be used as gate dielectric. The modeling of such devices can be done easily with the proposed self-consistent model.

In our calculations, we have used effective mass approximation for both electrons and holes. However, due to anisotropy and mixing of valance bands, the

use of effective mass approximation for holes has been a topic of debate. The present model for p-MOS devices may be further improved by incorporating the nonparabolicity of the valance band structure.

Bibliography

- [1] "The National Technology Roadmap for Semiconductors: Technology Needs," Semiconductor Industry Association, San Jose, California, 1997.
- [2] Farzin Assad, Zhibin Ren, Dragica Vasileska, Supriyo Datta and Mark Lundstrom, "On the performance limits for Si MOSFET's: A theoretical study," IEEE Trans. Electron Devices, Vol. 47, pp. 232-240, 2000.
- [3] F. Stern, "Self-consistent results for n-type Si inversion layers," Phys. Rev. B, Vol. 5, pp. 4891-4899, 1972.
- [4] S. M. Sze, *Physics of Semiconductor Devices*, Wiley Eastern Limited, pp. 362-366, 1987.
- [5] Y. Tsvividis, *Operation and Modeling of MOS Transistor*, MaGraw-Hill, Ch-2, 1999.
- [6] C. Moglestue, "Self-consistent calculation of electron and hole inversion charges at silicon-silicon dioxide interfaces," J. Appl. Phys., Vol. 59, pp. 3175-3183, 1986.
- [7] M. J. van Dort, P. H. Woerlee and A. J. Walker, "A simple model for quantisation effects in heavily-doped silicon MOSFETs at inversion conditions," Solid-State Electron., Vol. 37, pp. 411-414, 1994.
- [8] Scott A. Hareland, Shyam Krishnamurthy, Srinivas Jallepali, Choh-Fei Yeap, Khaled Hasnat, Al F. Tasch and Christine M. Maziar, "A computationally efficient model for inversion layer quantization effects in deep submicron n-channel MOSFET's," IEEE Trans. Electron Devices, Vol. 43, pp. 90-95, 1996.

- [9] G. Paasch, S. Scheinert and K. Tarnay, "Influence of inversion channel quantisation on the surface potential in the MOS structure," *Phys. Stat. Sol.*, Vol.149, pp. 751-755, 1995.
- [10] Luca Larcher, Paolo Pavan, Fabio Pellizzer and Gabriella Ghidini, "A new model of gate capacitance as a simple tool to extract MOS parameteres," *IEEE Trans. Electron Devices*, Vol. 48, pp. 935-945, 2001.
- [11] Shin-ichi Takagi and Akira Toriumi, "Quantitative understanding of inversion layer capacitance in Si MOSFET's," *IEEE Trans. Electron Devices*, Vol. 42, pp. 2125-2130, 1995.
- [12] S.-I. Takagi, M. Takayanagi and A. Toriumi, "Characterization of inversion layer capacitance of holes in Si MOSFET's," *IEEE Trans. Electron Devices*, Vol. 46, pp. 1446-1450, 1999.
- [13] S.-I. Takagi, M. Takayanagi, and A. Toriumi, "Impact of electron and hole inversion-layer capacitance on low voltage operation of scaled n- and p-MOSFET's," *IEEE Trans. Electron devices*, Vol. 47, pp. 999-1005, 2000.
- [14] C. Fiegna and A. Abramo, "Analysis of quantum effects in nonuniformly doped MOS structures," *IEEE Trans. on Electron Devices*, Vol. 45, pp. 877-880, 1998.
- [15] Douglas W. Barlage, James T. O'Keeffe, J. T. Kavalieros, M. M. Nguyen and R. S. Chau, "Inversion MOS capacitance extraction for high-leakage dielectrics using a transmission line equivalent circuit," *IEEE Electron Device letters*, Vol 21, pp. 454-456, 2000.
- [16] S. Jallepalli, J. Bude, W.-K. Shih, M. R. Pinto, C. M. Maziar and A. F. Tasch, "Electron and hole quantization and their impact on deep submicron silicon p- and n-MOSFET characteristics," *IEEE Trans. Electron Devices*, Vol. 44, pp. 297-302, 1997.
- [17] Y. T. Hou and Ming-Fu Li, "Hole quantization effects and threshold voltage shift in p-MOSFET-assumed by improved one-band effective mass approximation," *IEEE Trans. Electron Devices*, Vol. 48, pp. 1188-1193, 2001.

- [18] M. Giannini, A. Pacelli, A. L. Lacaita and L. M. Perron, "Effect of oxide tunneling on the measurement of MOS interface states," *IEEE Electron Device Lett.*, Vol. 21, pp. 405-407, 2000.
- [19] A. Pacelli, A. S. Spinelli and L. M. Perron, "Carrier quantization at flat bands in MOS devices," *IEEE Trans. Electron Devices*, Vol. 46, pp. 383-387, 1999.
- [20] Farhan Rana, Sandip Tiwari and D. A. Buchanan, "Self consistent modeling of accumulation layers and tunneling currents through very thin oxides," *Appl. Phys Lett*, Vol. 69, pp. 1104-1106, 1996.
- [21] S. H. Lo, D. A. Buchanan, Y. Taur and W. Wang, "Quantum-Mechanical modeling of electron tunneling current from the inversion layer of ultra-thin-oxide nMOSFET's," *IEEE Electron Device Lett.*, Vol. 18, pp. 209-211, 1997.
- [22] W.-K. Shih, E. X. Wang, S. Jallepalli, F. Leon, C. M. Maziar and A. F. Tasch, Jr., "Modeling gate leakage current in nMOS structures due to tunneling through an ultra-thin oxide," *Solid-State Electron.*, Vol. 42, pp. 997-1006, 1998.
- [23] Nian Yang, W. Kirklel Henson and J. J. Wortman, "Modeling study of ultrathin gate oxide using direct tunneling current and capacitance-voltage measurements in MOS devices," *IEEE Trans. Electron Devices*, Vol. 46, pp. 292-294, 1999.
- [24] S. Mudanai, Y.-Y. Fan, Q. Ouyang, A. F. Tasch and S. K. Banerjee, "Modeling of direct tunneling current through gate dielectric stacks," *IEEE Trans. Electron Devices*, Vol. 47, pp. 1851-1857, 2000.
- [25] Antonio Abramo, Andrew Cardin and Enrico Sangiorgi, "Two-dimensional quantum mechanical simulation of charge distribution in Silicon MOSEFTs," *IEEE Trans. Electron Devices*, Vol. 47, pp. 1858-1863, 2000.
- [26] A. Haque, A. Rahman and I. B. Chowdhury, "On the use of appropriate boundary conditions to calculate the normalized wave functions in the inversion layer of MOSFETs with ultra-thin gate oxides," *Solid-State Electron.*, Vol. 44, pp. 1833-1836, 2000.

- [27] S. Mudanai, L. F. Register, A. F. Tasch and S. K. Banerjee, "Understanding the effects of wave function penetration on the inversion layer capacitance of NMOSFETs," *IEEE Electron Device Lett.*, Vol. 22, pp. 145-147, 2001.
- [28] C. S. Lent and D. J. Kirkner, "The quantum transmitting boundary method," *J. Appl. Phys.*, Vol. 67, pp. 6353-6359, 1990.
- [29] A. Haque and A. N. Khondker, "An efficient technique to calculate the normalized wave functions in arbitrary one-dimensional quantum well structures," *J. Appl. Phys.*, Vol. 84, pp. 5802-5804, 1998.
- [30] A. N. Khondker and Muhammad A. Alam, "Buttiker-Landauer conductance formulas in the presence of inelastic scattering," *Phys. Rev. B*, Vol. 44, pp. 5444-5452, 1991.
- [31] A. N. Khondker, M. R. Khan and A. F. M. Anwar, "Transmission line analogy of resonance tunneling phenomena: the generalized impedance concept," *J. Appl. Phys.*, Vol. 63, pp. 5191-5193, 1988.

Appendix A

The modified self-consistent model, which has been used in this study, has been described in section 2.3. Here, some important points, which should be followed to get better results and save valuable computational time, are highlighted. At the end, the whole self-consistent model is presented in flowchart form.

A.1 Brief Description of Calculation

In our self-consistent calculation, N_{inv} is the independent variable. For analysis at room temperature one has to start with a lower value of N_{inv} ($\sim 10^8 \text{ cm}^{-2}$) then gradually go to higher values. As the number of points increased, so does the accuracy, but at the cost of increased computational time. Since the modeling of threshold region depends critically on the number of N_{inv} points selected, the standard practice is to choose much closer values of N_{inv} near the threshold region, but in the sub-threshold region or strong inversion region the values need not be so close.

As the self-consistent solution is an iterative technique, a better initial guess provides quicker convergence. So, the semi-classical model can be used to give a better initial guess to start the analysis with a very low N_{inv} . For a certain N_{inv} , the value of Φ_d can be calculated using the depletion approximation and the whole procedure is give in detail in Ref.[5].

After defining the total MOS structure as shown in Fig. 1.1, for numerical calculation, the system should be sub-divided into small grids in the Z direction. An important decision to make is how many grids one should choose in different regions. Higher the no. of grids, more accurate will be the numerical results,

but in expense of a proportionately increased computational time. As the wavefunction mainly concentrates in the inversion region (*i.e.* region in silicon near the Si/SiO_2 interface), for more accurate simulation, the no. of grids should be high in that region. But in metal or deep inside the semiconductor the grids may be small in no.. So, the above decision can optimize the results as well as computational time.

Some times, due to numerical reasons, the loop may diverge or fluctuate around a point. To avoid such problems, a weighting factor can be incorporated which will construct the new potential profile by taking an weighted average of the new and the old potential profiles.

15856

A.2 Flowcharts

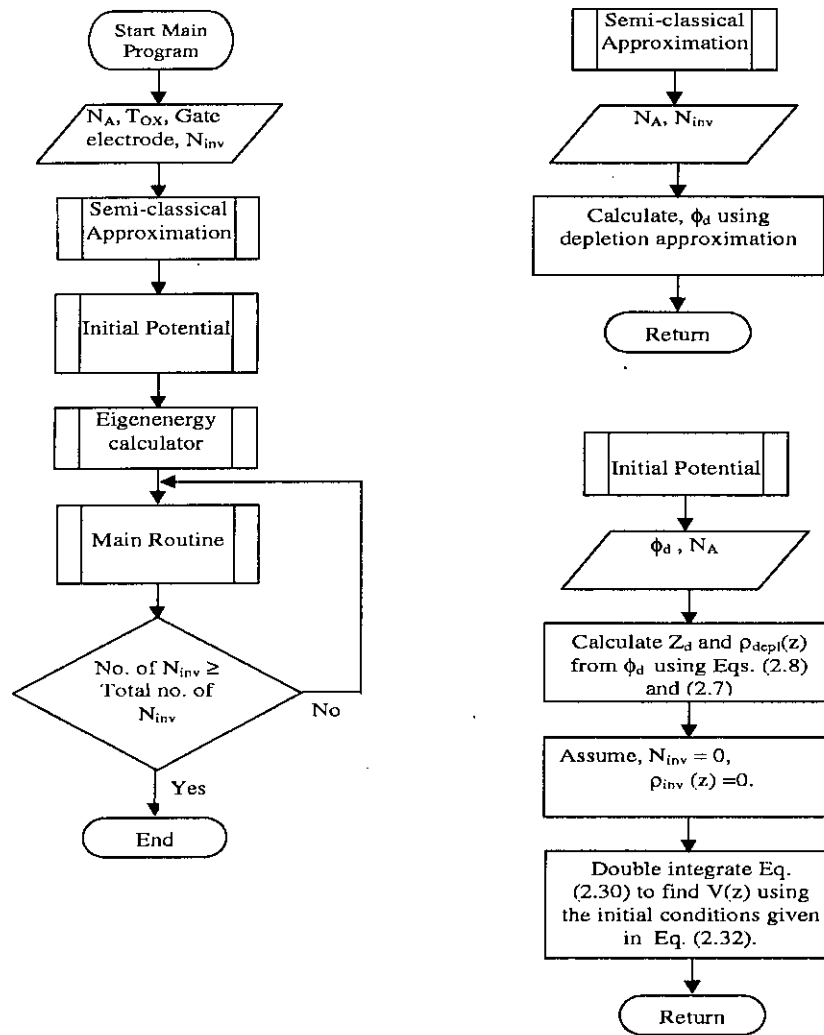


Fig. A.1: Flowchart.

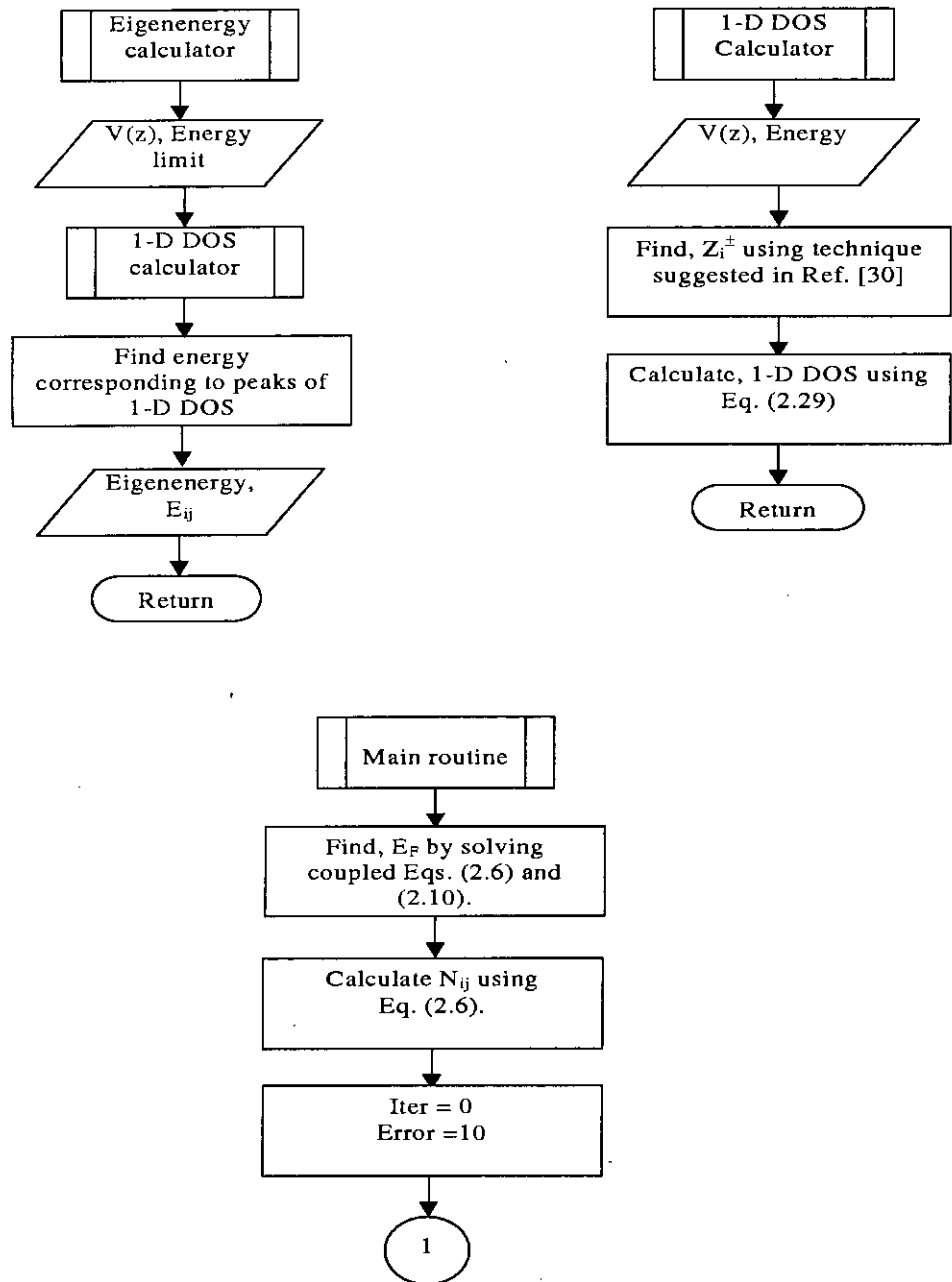


Fig. A.2: Flowchart (continued).

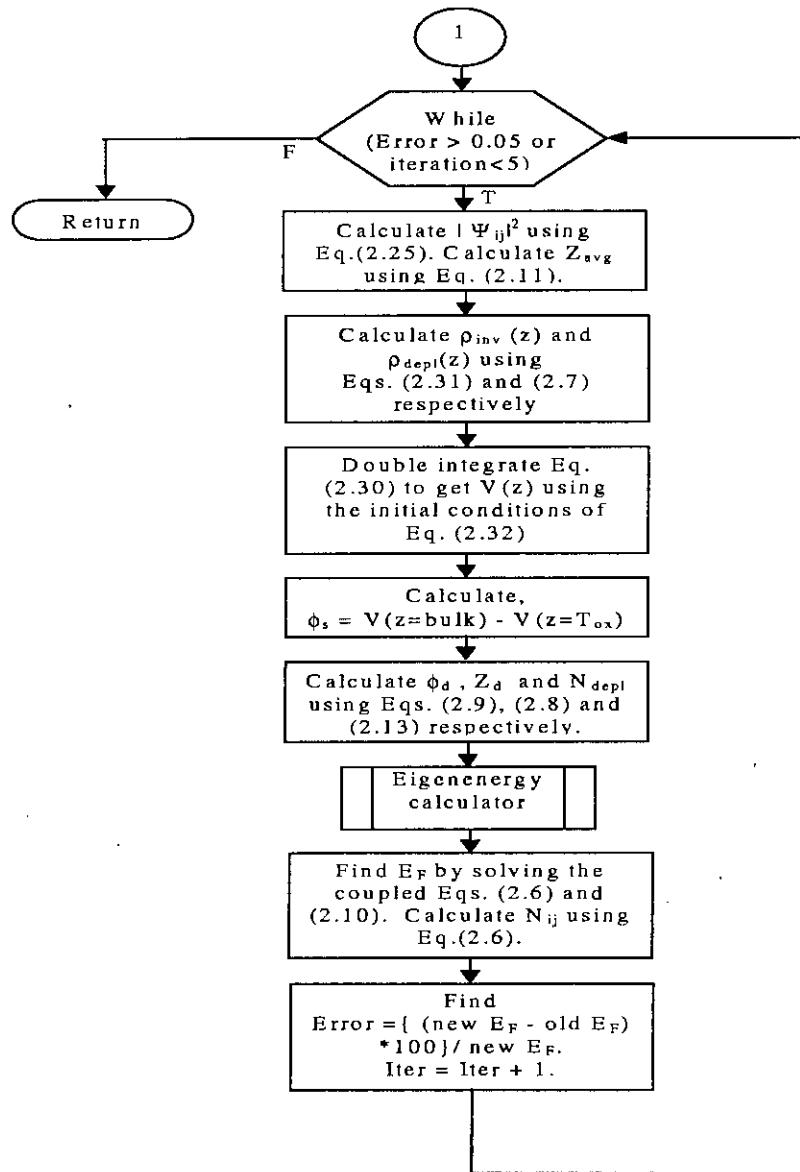


Fig. A.3: Flowchart (continued).

